



HAL
open science

Lipid bilayers: Phase behavior and nanomechanics

Lorena Redondo-Morata, Patricia Losada-Pérez, Marina Inés Giannotti

► **To cite this version:**

Lorena Redondo-Morata, Patricia Losada-Pérez, Marina Inés Giannotti. Lipid bilayers: Phase behavior and nanomechanics. Irena Levitan; Andreea Trache. Membrane Biomechanics, 86, Elsevier, pp.1-55, 2020, Current Topics in Membranes, 978-0-12-821021-5. 10.1016/bs.ctm.2020.08.005 . hal-02976730

HAL Id: hal-02976730

<https://hal.science/hal-02976730>

Submitted on 23 Oct 2020

HAL is a multi-disciplinary open access archive for the deposit and dissemination of scientific research documents, whether they are published or not. The documents may come from teaching and research institutions in France or abroad, or from public or private research centers.

L'archive ouverte pluridisciplinaire **HAL**, est destinée au dépôt et à la diffusion de documents scientifiques de niveau recherche, publiés ou non, émanant des établissements d'enseignement et de recherche français ou étrangers, des laboratoires publics ou privés.

1 Lipid bilayers: phase behavior and 2 nanomechanics

3 **LORENA REDONDO-MORATA**

4 *Center for Infection and Immunity of Lille, INSERM U1019, CNRS UMR 8204, F-59000 Lille, France.*

5 **PATRICIA LOSADA-PÉREZ**

6 *Experimental Soft Matter and Thermal Physics (EST) group, Department of Physics, Université
7 Libre de Bruxelles, 1050 Brussels, Belgium*

8 **MARINA INÉS GIANNOTTI**

9 *Biomedical Research Networking Center on Bioengineering, Biomaterials and Nanomedicine
10 (CIBER-BBN), Spain.*

11 *Institut de Bioenginyeria de Catalunya (IBEC), The Barcelona Institute of Science and Technology
12 (BIST), 08028 Barcelona, Spain.*

13 *Departament de Ciència de Materials i Química Física, Universitat de Barcelona, 08028
14 Barcelona, Spain.*

15 miannotti@ibecbarcelona.eu

16

17 **Keywords:**

18 *Lipid phase behavior / phase transition / phase coexistence / nanomechanics / thermodynamics
19 / Atomic Force Microscopy (AFM)/ Quartz crystal microbalance with dissipation monitoring
20 (QCM-D)*

21

22 Contents

23	1. Abstract	- 2 -
24	2. Introduction	- 3 -
25	3. Experimental approaches to study membrane mechanics.....	- 5 -
26	3.1. Model systems: supported vesicles layers (SVLs) lipid bilayers (SLBs)	- 5 -
27	3.1 QCM-D.....	- 7 -
28	3.2. Atomic Force Microscopy (AFM)-based methodology	- 11 -
29	4. Phase behavior and nanomechanics. From one component membranes to higher complexity	
30	- 18 -
31	4.1. One-component membranes.....	- 18 -
32	4.1.1. The gel and the fluid phase	- 18 -
33	4.1.2. The thermal transition	- 22 -
34	4.2 Phase coexistence	- 26 -
35	1.2. The role of cholesterol	- 32 -
36	5. Connection between nanoscale measurements and thermodynamic descriptors of	
37	membranes	- 37 -
38	6. Conclusions and future perspectives	- 38 -
39	7. Acknowledgements.....	- 39 -
40	8. Glossary of lipid acronyms	- 39 -
41	9. References.....	- 40 -
42		

43 1. Abstract

44 Lipid membranes are involved in many physiological processes like recognition, signaling, fusion
45 or remodeling of the cell membrane or some of its internal compartments. Within the cell, they
46 are the ultimate barrier, while maintaining the fluidity or flexibility required for a myriad of
47 processes, including membrane protein assembly. The physical properties of *in vitro* model
48 membranes as model cell membranes have been extensively studied with a variety of
49 techniques, from classical thermodynamics to advanced modern microscopies. Here we review
50 the nanomechanics of solid-supported lipid membranes with a focus in their phase behavior.
51 Relevant information obtained by quartz crystal microbalance with dissipation monitoring
52 (QCM-D) and atomic force microscopy (AFM) as complementary techniques in the
53 nano/mesoscale interface is presented. Membrane morphological and mechanical
54 characterization will be discussed in the framework of its phase behavior, phase transitions and
55 coexistence, in simple and complex models, and upon the presence of cholesterol.

2. Introduction

56
57
58
59
60
61
62
63
64

65
66
67
68
69
70
71
72
73
74

75
76
77
78
79
80
81
82
83
84
85
86
87

Cells can be thermodynamically defined as open systems in constant exchange of mass, energy and information with the environment. The membrane is the ultimate boundary for the cell, confining it from the medium and some of its internal compartments. The cell membrane is a fundamental structure of the cell, providing a support matrix for proteins and carbohydrates. As complex systems, cell membrane performance is the result of lipids and proteins working together, with main functions like being barriers, mediating the exchange of molecules and information, promoting signaling and adhesion, and being metabolically self-renewing structures.

Cell membranes are materials with unique physical properties allowing cells to rapidly change shape, squeeze, stretch, pinch off smaller units, fuse, and reseal. This is the result of being viscous sheets with both fluid and elastic properties. Cell membranes are supramolecular structures, where the lipids and proteins interact through non-covalent bonding. Membranes are curved surfaces, vesicular in nature, whose curvature is deeply influenced by the lipid packing. The lipid bilayer, made of millions of building blocks held together by weak interactions, is in part responsible for the physical, dynamic and mechanical properties of the cell membrane. In the membrane, lipids are mainly organized in lamellar phases, where two leaflets of lipids are self-assembled exposing the polar headgroups to the aqueous interface and keeping the fatty-acyl chains aligned opposed and parallel to one another to form the hydrophobic core.

The enterprising scientist Alec Bangham was the discoverer in 1958 of the ‘multilamellar smectic mesophases’ or, as himself referred to less seriously, the ‘bangasomes’ (Bangham et al., 1958) - which were eventually named ‘liposomes’ to define microscopic lipid vesicles (Sessa & Weissmann, 1968). When the Babraham Institute (Cambridge, UK) acquired its first electron microscope in 1961, Bangham had the privilege to firstly observe the dispersions of phospholipids in water solutions of negative stains (Bangham & Horne, 1964). In the following years, Bangham and his collaborators performed the key experiments to demonstrate that lipid bilayers maintain concentration gradients of ions such as potassium and sodium. Indeed, David D. Deamer wrote in his memoir *“It was the membrane equivalent of finding the double helix structure of DNA, another Cambridge discovery in the life sciences”* (Deamer, 2010). This was reflected in the well-known lecture by Bangham in the University of Bristol in 1975, entitled “Membranes came first”, where he proposed that something similar to liposomes had been available to house the first forms of life. Indeed, all living organisms have a membrane.

88 Later in the early 1970s, Singer and Nicolson proposed the fluid-mosaic-model, depicting the
89 cell membranes as two-dimensional liquids where all lipid and protein molecules diffuse easily
90 (Singer & Nicolson, 1972). Concerning the composition, besides all the proteins and
91 carbohydrates, lipids are the main components of the cell membrane in terms of molar fraction.
92 Lipids are a broad family which covers many different chemical structure sphingolipids
93 (ceramides, sphingomyelin, gangliosides, sphingosines), sterols (cholesterol and vitamins), and
94 phospholipids, each of them contributing to different and crucial physicochemical properties.

95 Gradual progress was made in the knowledge of the complexity of the biological membranes.
96 The most famous hypothesis in the field is the membrane raft proposed in 1997 by K. Simons
97 and E. Ikonen (Simons & Ikonen, 1997). The idea was based on the fact that portions of
98 membrane were found to be detergent resistant, that may give rise to a virtual
99 compartmentalization of the cell. This hypothesis generated a lot of literature and became a
100 recursive concept in the field. Nowadays it is well known that there is a variety of nanostructures
101 in the membrane of heterogeneous sizes and functions, and the methods that allow us to
102 observe these nanodomains *in vivo* are only beginning to emerge (Goñi, 2019b; Pinkwart et al.,
103 2019). Nanodomains can be considered putative heterogeneous structures within the
104 membrane which are due partly to phase separation.

105 The mechanical role of the lipid membrane in force-triggered and force-sensing mechanisms in
106 cells is of significance and adds to the better-established role of the mechanosensitive proteins
107 (Vogel, 2006)(Kechagia et al., 2019). Membrane conformational changes such as bending,
108 vesiculation or tubulation are involved in cellular processes including adhesion, signaling,
109 endocytosis or membrane resealing (van Meer & de Kroon, 2011)(van Meer et al.,
110 2008)(Hassinger et al., 2017). For instance, in endocytosis, the endocytic system needs to
111 generate enough force to form an endocytic vesicle by bending the membrane. These
112 mechanisms generally require the membrane separation from the cytoskeleton as well as strong
113 bending, for which the membrane chemical composition and physicochemical properties, often
114 highly localized and dynamic, are key players (Sheetz, 2001)(van Meer et al., 2008). It is now
115 clear that the lipid packing and composition are direct modulators of the membrane curvature
116 and elasticity, at different scales, even locally at the nanometer scale (Yeagle, 1989)(Vereb et
117 al., 2003). Understanding the lipid bilayers structural and mechanical properties and the
118 involvement and role of each individual component turns out to be essential in order to identify
119 their contribution to the overall membrane traits. Structural and physical properties of lipid
120 bilayers include shape and local distribution of components (phases and domains), and related
121 mechanical stability in response to compression, bending or stretching, their ability to fuse, etc.

122 We review the nanomechanics of solid-supported lipid membranes and how these relate to lipid
123 membrane phase behavior. To this end, we chose two complementary techniques with
124 nano/mesoscale sensitivity to mechanical and viscoelastic properties, namely quartz crystal
125 microbalance with dissipation monitoring (QCM-D) and atomic force microscopy (AFM). QCM-D
126 is a label-free surface-sensitive technique, whose working principle is based on the inverse
127 piezoelectric effect. Real-time simultaneous measurements of resonant frequency and energy
128 dissipation make QCM-D very suitable for gravimetric and viscoelastic characterization of solid-
129 supported nanoscale sized films. AFM is a technique that allows the observation of surfaces
130 under controlled liquid environment, to resolve topographical features with nanoscale
131 resolution and to measure and apply forces in the pN-nN range. Therefore, AFM is appropriate
132 for imaging the topography of solid-supported lipid membranes and probing the physical and
133 mechanical properties at the nanoscale by means of force spectroscopy, providing high spatial
134 and force resolution. QCM-D is complementary to AFM, useful for probing changes in
135 viscoelastic properties during solid-supported film formation. The complementarity of AFM and
136 QCM-D manifests at different levels: i) AFM measurements are performed at a local level, while
137 QCM-D provides a global characterization of the solid-supported films; ii) both techniques
138 enable dynamic mechanical analysis by applying a small oscillatory stress, however, the AFM tip
139 scans and deforms supported layers from the top, whereas QCM-D measures the sensor
140 oscillation from the bottom. The combination of AFM and QCM-D for supported lipid
141 membranes has been employed in previous works (see, for instance (R. Richter et al., 2003,
142 2003; Van Lehn et al., 2014). In the following sections we briefly describe the membrane models
143 and discuss the working principles behind both approaches, highlighting the quantitative and
144 qualitative mechanical information that can be extracted using each technique. Specific
145 examples on the usefulness to monitor phase transitions on one-component to more complex
146 bilayers, and resolve domain coexistence are also provided, including the key role of cholesterol.

147 3. Experimental approaches to study membrane mechanics

148 3.1. Model systems: supported vesicles layers (SVLs) lipid bilayers (SLBs)

149 Due to the extreme complexity of biological membranes, cell membrane mimetics are excellent
150 approaches to study membrane properties and biological processes at the cellular and
151 subcellular level. A great deal of what we know about these processes comes from modeling
152 lipid bilayers *in vitro*. Various membrane systems are established as biomimetic structures. They
153 include vesicles: freely-suspended and supported liposomes, giant unilamellar vesicles (GUVs);
154 micelles, bicelles; suspended and supported lipid films: Langmuir monolayers, phospholipid
155 bilayers nanodiscs, black lipid membranes (BLM), supported lipid bilayers (SLB), tethered bilayer

156 lipid membranes (tBLM), polymer-cushioned membranes, protein-tethered bilayer lipid
157 membranes (ptBLM) and hybrid bilayers (Sebaaly et al., 2019)(Dimova, 2019)(Doktorova et al.,
158 2018)(Siontorou et al., 2017)(Rascol et al., 2016). Among these, the giant unilamellar vesicles
159 (GUVs) have been extensively used since they offer a perfect stage to study the mechanical,
160 thermodynamic, electrical, and rheological properties of the overall GUV and lipid bilayer as a
161 function of membrane composition, surrounding media and temperature (Dimova, 2019)(Evan
162 Evans et al., 2003)(Kahya et al., 2004). Being heterogeneous and dynamic at the nanoscale,
163 nanotechnology-based techniques can further explore biomembranes locally with resolution at
164 the nanometric level. For many of these techniques, like surface analytical techniques, solid-
165 supported models are the most adequate, including supported lipid monolayers, supported
166 vesicles layers (SVLs) or supported lipid bilayers (SLBs).

167 SVLs are the precursor solid-supported systems to planar SLBs formed by vesicle fusion and
168 rupture. They result from spontaneous adsorption of small vesicles of diameter $d \leq 200$ nm onto
169 solid surfaces. The geometry of SVLs embodies membrane curvature, tension and osmotic stress
170 within the supported layer. This makes SVLs useful biomimetic platforms to probe membrane
171 deformation using surface-sensitive techniques and testing ground for adhesion, budding and
172 lipid membrane exchange and fusion (Lipowsky & Seifert, 1991; Hurley et al., 2010; Tabaei et
173 al., 2016; Steinkühler et al., 2019). SVLs are generally formed by small soft adsorbates which are
174 mimics to small endosomes or exosomes. These are optically inaccessible systems and the
175 experimental investigation of their deformation is not straightforward. Adsorbed vesicles onto
176 inorganic surfaces also serve as model systems relevant to biocompatibility studies. Vesicle
177 adsorption is very often accompanied by vesicle deformation upon contact with the solid
178 support. The extent of vesicle deformation depends on several factors such as vesicle size,
179 mechanical properties of the vesicles, adhesion strength of the surface, osmotic pressure
180 difference over the vesicle, etc. The fate of vesicles upon adsorption on a solid support depends
181 both on vesicle-vesicle and vesicle surface interactions. In the absence of osmotic stress and at
182 a concentration where vesicle surface coverage enhances fusion probability, the rupture of
183 vesicles will depend strongly on the adhesion strength. Specifically on how this imbalances the
184 energetic competition between adhesion energy and an elastic stretching of the membrane
185 (Lipowsky & Seifert, 1991). If the adhesion strength W is large enough and exceeds the lysis
186 tension of the membrane, the vesicles will rupture. SVLs are typically formed on surfaces whose
187 adhesion strength is not sufficient to induce vesicle rupture, such as Au, TiO₂, Pt (Tero, 2012).

188 SLBs are very manageable platforms relatively simple to obtain and that retain two-dimensional
189 order and lateral mobility. They are ideal to study lipid lateral interactions and membrane local

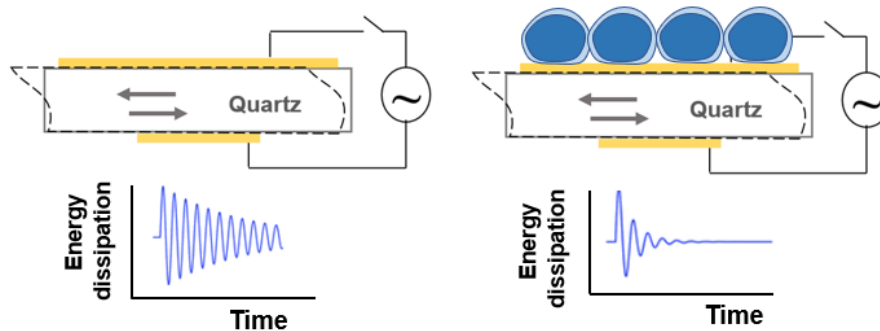
190 mechanical properties, growth of lipid domains, as well as interactions between the lipid
191 membrane and proteins, peptides and drugs, cell signaling, etc. They also offer an excellent
192 environment for inserting membrane proteins. There are many different methods that can be
193 used to obtain SLBs, like the spin-coating and hydration (Mennicke & Salditt, 2002),
194 microcontact printing (Strulson & Maurer, 2011), solvent-exchange deposition (Tabaei et al.,
195 2016; Hohner et al., 2010), and the most widely used methods like the Langmuir–
196 Blodgett/Schäfer deposition to prepare mono and bilayers (Kurniawan et al., 2018), and the
197 liposome fusion and rupture method for bilayers (Hardy et al., 2013)(Mingeot-Leclercq et al.,
198 2008). The liposome rupture method remains the most popular and simple one, based on
199 depositing small unilamellar vesicles (SUVs) from a suspension onto a flat substrate where the
200 adhesion strength is high, generally mica or silicon oxide, but can also be formed on bare or
201 gold-coated glass, following the needs of the analysis technique (Mingeot-Leclercq et al., 2008;
202 Ralf P Richter & Brisson, 2005)(Choi et al., 2016; B. Gumí-Audenis et al., 2018; Seeger et al., 2010;
203 Winkler et al., 2020). Once in contact with the substrate the SUVs start fusing between them,
204 deforming, flattening, and finally rupturing to form a continuous film. It is important to have in
205 mind that the final SLB structure is affected by variables like the lipid vesicles composition,
206 concentration, and size, the physicochemical environment pH, temperature, and ionic strength,
207 as well as the surface roughness and charge density (Reimhult et al., 2003).

208 3.1 QCM-D

209 Quartz crystal microbalance with dissipation monitoring (QCM-D) is an acoustic-based surface-
210 sensitive technique that enables label-free, real-time simultaneous measurements of wet-mass
211 and viscoelastic properties of solid-supported nano/meso-scaled adlayers.

212 The QCM-D sensor consists of an AT-cut quartz crystal being sandwiched between two
213 electrodes. When an AC voltage is applied across the electrodes with a frequency close to the
214 resonant frequency of the quartz crystal, a mechanical deformation is induced, resulting in a
215 standing shear wave. The surfaces of the electrodes coincide with the antinodes of the standing
216 shear wave with wavelength $\lambda = 2d / n$, with d the quartz thickness and n the (odd) overtone
217 number. The resonance frequency at each overtone is $f_n = nv / 2d$, with v the speed of sound in
218 quartz. The shear waves propagate as evanescent waves decaying across the boundary between
219 the crystal and the fluid environment (air or liquid) with a penetration depth $\delta = \sqrt{\eta_L / \pi f_n \rho_L}$,
220 which depends on the overtone frequency f_n and on the viscosity η_L and density ρ_L of the fluid in
221 contact with the sensor surface (Reviakine et al., 2011). The penetration depth of a 5 MHz shear
222 wave in water is $\delta \sim 250$ nm, rendering QCM-D surface-specific. D is defined as the ratio

223 between the dissipated energy during one vibration period and the total energy of the crystal at
 224 that instant $D = E_{lost} / 2\pi E_{stored}$. In the so-called ‘ring-down method’ measurements, energy
 225 dissipation D can be calculated when the AC voltage driving the quartz crystal oscillation is
 226 turned off. The working principle of QCM-D is reflected in Figure 1, upon the presence of a soft,
 227 viscoelastic layer such as a layer of lipid SVLs. The amplitude of the crystal oscillation decays
 228 exponentially and much faster when in contact with a viscoelastic layer, characterized by a large
 229 energy dissipation response.



230

231 **Figure 1.** Schematic view of a QCM-D sensor excited by an AC voltage. Left panel: Bare Au-coated
 232 sensor in liquid environment, the dampening of the oscillations takes place slowly. Right panel:
 233 The presence of an adsorbed lipid vesicle layer (SVL) induces a faster damping of the oscillations
 234 and thus a larger energy dissipation.

235 Commercial QCM-D instruments allow for monitoring changes in frequency and dissipation for
 236 several overtones ($n = 3, 5, 7, \dots, 13$), Δf_n and ΔD_n , upon the presence of a nano/mesoscale layer.
 237 The spectroscopic data at multiple frequencies with varying detection range enables assessing
 238 the spatial homogeneity and rigidity of the adsorbed layer. For homogeneous thin and rigid
 239 films, $\Delta D_n \sim 0$, Δf_n overtones overlap and a simple relationship between mass adsorbed and
 240 change in frequency holds, the so-called Sauerbrey relation: $\Delta m = -C\Delta f / n$, with C being the
 241 Sauerbrey constant which for a 5 MHz quartz crystal reads $C = d\rho_{quartz} / f_0 = 17.7 \text{ ng/cm}^2$
 242 (Sauerbrey, 1959). For thicker and softer films $\Delta D_n > 0$, overtones do not overlap and the
 243 ensemble quartz-film-fluid can be represented by simple models combining elastic components
 244 and viscous dashpots. These models enable to extract effective viscoelastic parameters of the
 245 adsorbed film such as shear viscosity, thickness and shear storage modulus (Cho et al., 2007;
 246 Voinova et al., 1999).

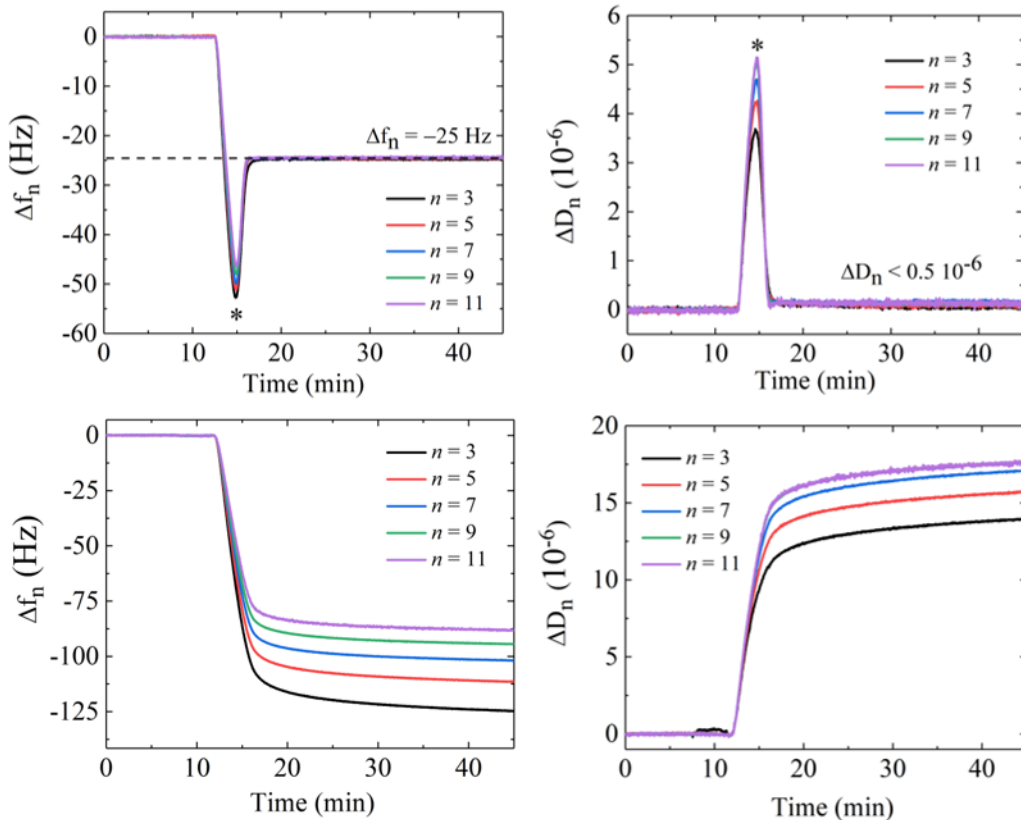
247 The capability of monitoring the viscoelastic properties during film formation is particularly
 248 useful in the case of solid-SLB formation. QCM-D has been a valuable tool in deciphering the
 249 kinetic pathways of SLB formation from precursor vesicles and how those depend on relevant

250 conditions such as solid surface adhesion strength, medium ionic strength, vesicle mechanics,
251 etc. (Cho et al., 2010; Jing et al., 2013; C. A. Keller & Kasemo, 1998; Pramanik et al., 2016; R P
252 Richter, 2006).

253 Figure 2 shows a typical QCM-D experiment where real-time monitoring of the adsorption of
254 zwitterionic DOPC vesicles onto SiO₂ and oxidized Au was carried out at 37 °C. The vesicles are
255 dispersed in TRIS-buffer (10 mM TRIS, 100 mM NaCl, pH 8) at a concentration of 0.1 mg/mL and
256 their hydrodynamic diameter $d = 79 \pm 20$ nm. As initially discussed by Keller and Kasemo (C. A.
257 Keller & Kasemo, 1998), the adsorption kinetics is surface-specific. The mechanistic picture of Δf
258 and ΔD changes is governed by a delicate balance between the adhesive contribution to the free
259 energy from lipid-surface interactions and the opposing effect of bending and stretching the
260 membrane (Lipowsky & Seifert, 1991). DOPC vesicles adsorbing on SiO₂ follow a two-step
261 adsorption process consisting of i) adsorption of a critical number of vesicles and ii) fusion,
262 rupture and formation of an SLB. This is reflected in the Δf_n and ΔD_n signals depicted in the upper
263 panels of Figure 2. After a ~ 10 min baseline in buffer (Δf_n and $\Delta D_n = 0$), DOPC vesicles added at
264 a very small flow rate adsorb onto the SiO₂-coated quartz sensor (Δf_n decreases and ΔD_n
265 increases) until a maximum number (minimum in Δf_n and maximum in ΔD_n). Adsorbed vesicles
266 then fuse and rupture as a consequence of the large adhesion strength of SiO₂, thus releasing
267 the entrapped aqueous buffer. As a consequence, Δf_n increases (mass loss) to a constant plateau
268 of $\Delta f_n \sim -25$ Hz and the ΔD_n signal decreases back to a very small value ($\Delta D_n < 0.5 \cdot 10^{-6}$). The final
269 Δf_n and ΔD_n values and the fact that overtones signals overlap is consistent with the formation
270 of a homogeneous rigid and thin DOPC SLB. The pathway of SLB formation is not unique and
271 depends strongly on the ionic conditions (head group charges of the constituent lipids, buffer
272 ionic strength presence of divalent cations, pH). Vesicles containing positively charged lipids like
273 DOTAP SUVs rupture individually on SiO₂ as a consequence of stronger vesicle-support
274 electrostatic interactions (R. Richter et al., 2003).

275 When DOPC vesicles adsorb onto an oxidized Au surface, a monotonic Δf_n decrease and ΔD_n
276 increase can be observed reaching constant non-zero plateau values with non-overlapping
277 overtones. Such time-dependent responses provide evidence that oxidized Au facilitates non-
278 ruptured vesicle adsorption towards the formation of acoustically non-rigid vesicle layers with
279 saturated coverage. As pointed out by Lind and Cárdenas (Lind & Cárdenas, 2016), it is worth
280 mentioning that local vesicle rupture events and formation of small bilayer patches cannot be
281 ruled out. As a matter of fact, QCM-D is very sensitive to hydrodynamic (wet) mass and the local,
282 partial formation of SLBs might be masked by the adsorption of vesicles on top or in between
283 the bilayer patches. In this case, complementary QCM-D and AFM measurements are

284 particularly useful to obtain a complete picture of the heterogeneous layers SLBs with co-
 285 adsorbed vesicles formed. For example, the complementarity of AFM and QCM-D has proven
 286 successful in experimentally confirming defect (protrusion)-driven nanoparticle interactions
 287 with SLBs (Van Lehn et al., 2014).

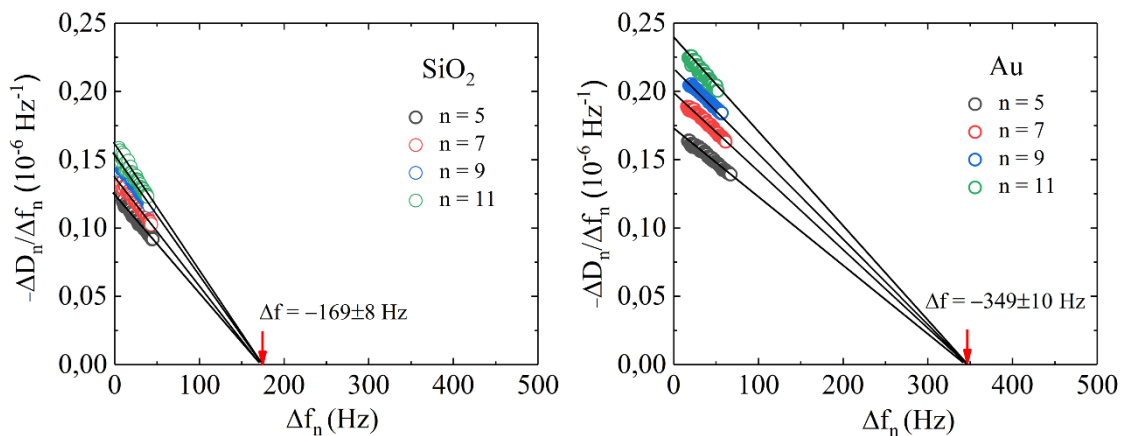


288

289 **Figure 2.** Time dependence of Δf_n and ΔD_n during a QCM-D experiment of DOPC vesicle adsorption
 290 at 37°C onto SiO₂ (upper panels) and Au (lower panels).

291 Apart from kinetic information, QCM-D can be also useful to estimate the extent of vesicle
 292 deformation upon adsorption following a model-free approach introduced by Tellechea *et al.*
 293 (Tellechea et al., 2009). This method consists in plotting $-\Delta D/\Delta f$ ratio vs $-\Delta f$ for all overtones
 294 during initial adsorption, which shows a linear decrease over a large range of frequency shifts.
 295 Extrapolation of this linear decrease to a frequency-independent intercept with the $-\Delta f$ axis
 296 (where overtones intersect) provides a value of the thickness of the adsorbed vesicle layer h or
 297 Sauerbrey thickness: $h = -\Delta f C / \rho$, where $C = 17.7 \text{ ng/cm}^2 \text{ Hz}$ and $\rho = 1 \text{ g/cm}^3$ is the density of
 298 the film. This approach assumes a complete surface coverage, where the presence of trapped
 299 buffer has been diminished to occupy only the void spaces between densely packed vesicles (the
 300 $-\Delta D/\Delta f$ ratio is close to zero and the $-\Delta f$ intercept values were the same on the extrapolation of
 301 a linear regression) (Tellechea et al., 2009; Reviakine et al., 2012; Olsson et al., 2013). Figure 3

302 displays the extrapolated Sauerbrey thickness for DOPC SUVs adsorbed onto SiO₂ and Au
 303 surfaces. The respective effective frequencies read $h(\text{SiO}_2) = 30 \pm 2$ nm and $h(\text{Au}) = 62 \pm 5$ nm. If
 304 one compares these values with the original vesicle diameter in bulk measured by DLS ($d = 79 \pm$
 305 20 nm), vesicles were deformed to a greater extent onto SiO₂ surfaces. A more exact approach
 306 based on a hydrodynamic model was recently introduced by Cho and co-workers (Gillissen et
 307 al., 2017) to estimate the deformation of small vesicles at low surface coverage. The model
 308 enables to estimate adsorbed vesicle shape and bending energy by using hydrodynamic
 309 spectroscopy (frequency shifts at several overtones). It treats vesicles as ellipsoids and relates
 310 the so-called QCM-D force to the scaled viscous penetration depth δ/a with δ the viscous
 311 penetration depth, and a the non-deformed vesicle radius, in order to probe the adsorbed
 312 particle aspect ratio. Further details on the model can be found in (Gillissen et al., 2017).

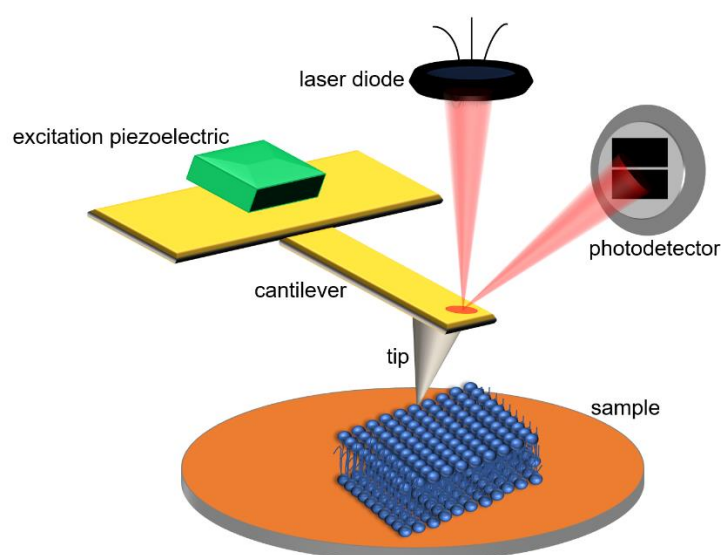


313
 314 **Figure 3.** $\Delta D_n / -\Delta f_n$ ratio as a function of frequency at different overtones for DOPC vesicles
 315 adsorbed onto SiO₂ and Au.

316 3.2. Atomic Force Microscopy (AFM)-based methodology

317 Classical structural techniques such as X-ray, NMR or electron microscopy rely on ensemble
 318 averaging of molecular properties. Yet, by these means, the underlying molecular dynamics can
 319 be hidden, since the signal comes from the average of many unsynchronized molecules in the
 320 bulk. The picture changes when using single-molecule techniques. The measured signal of one -
 321 or a few- molecules reflects the stochasticity of thermally induced processes when randomly
 322 crossing free-energy barriers. Single-molecule optical microscopy techniques are particularly
 323 well suited for the study of the dynamics of molecules. However, these latter methods rely on
 324 the detection of fluorescent markers attached to proteins or lipids, which means that the
 325 resolution is limited to ~ 200 nm due to diffraction of light and to a few tens of nm thanks to
 326 super-resolution techniques. The atomic force microscopy (AFM) was since its invention in 1986
 327 (Binnig et al., 1986) quickly positioned among the single-molecule, high-resolution structural

328 analysis techniques. It provides information concerning structure, function-related
329 conformational changes and supramolecular assemblies, crucial for a complete understanding
330 of biological processes. Nowadays, AFM is in its thirties and has become an invaluable tool for
331 studies at the micro- and nanoscale. As a stand-alone, high-resolution imaging technique and
332 force transducer, it is today an established methodology among the biophysical community. The
333 AFM uses a nanometer-sharp tip -resembling a record player needle- attached to a
334 (micro)cantilever to sense the sample surface while scanning it using piezoelectric elements. An
335 optical system is used to detect the cantilever deflection (or force), thanks to a laser diode beam
336 reflected on the back of the cantilever and detected by a photodiode. Changes in deflection due
337 to sample protrusions while the tip scans the sample are translated into electrical signals thanks
338 to a feedback mechanism. This is schematically represented in Figure 4.



339

340 **Figure 4.** Schematic representation of an AFM instrument. The deflection of the cantilever in the
341 normal direction is monitored by a photodetector which collects the reflection of a laser beam
342 focused at the back of the AFM cantilever. In the tapping mode, thanks to a piezoactuator, the
343 AFM cantilever is excited near its resonance frequency.

344 One of the main strengths of AFM relies on the possibility of working in a controlled environment
345 (medium composition and temperature) and with great spatial resolution. AFM-imaging mode
346 provides submolecular resolution on a large variety of biological samples: from single molecules,
347 that is, DNA or proteins, to supramolecular assemblies such as SLBs, or even entire cells (Giles
348 et al., 1993)(Dufrêne et al., 2017; Parot et al., 2007). Therefore, AFM has become a well-
349 established technique for imaging the topography of lipid membranes that show homogeneous
350 or phase-separated morphology, permitting then to increase the bilayer complexity, from

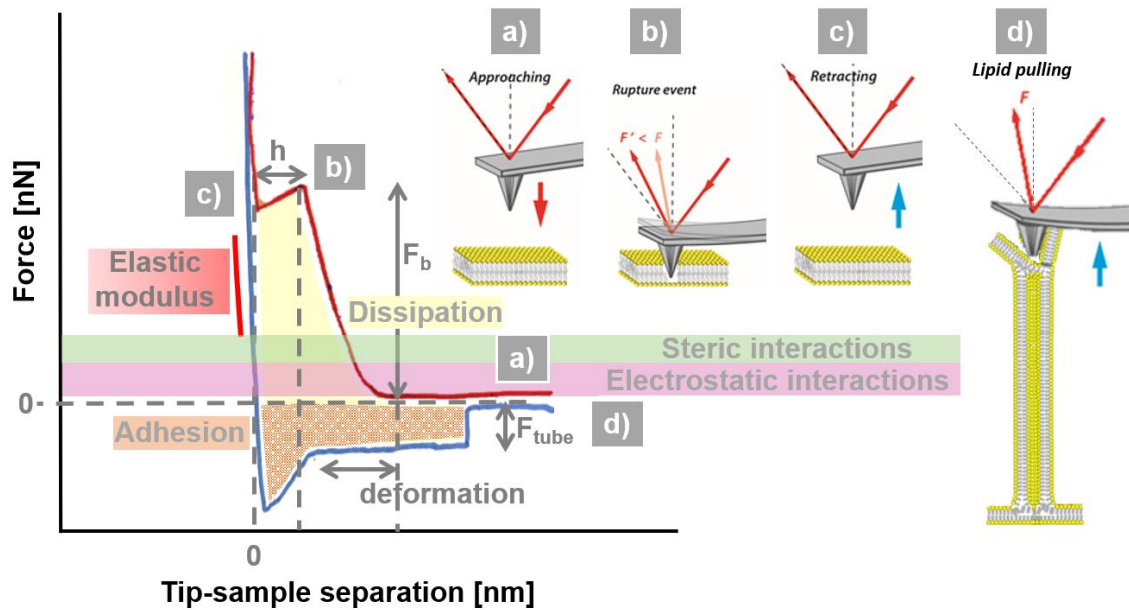
351 bilayers of one component to multicomponent ones (El Kirat et al., 2010; B. Gumí-Audenis et al.,
352 2016a; Morandat et al., 2013; L Redondo-Morata et al., 2014).

353 For the study of biological samples, it is common to use AFM-imaging dynamic modes that have
354 an intermittent tip-sample contact. Among them, the most often used is oscillation or tapping
355 mode, in which the AFM cantilever is excited near its resonance frequency. The resulting
356 oscillating tip is intermittently contacting -tapping- the surface, giving rise to a damped
357 oscillation amplitude. Additionally, the resonance frequency is also shifted due to the probe-
358 surface interaction. The topography of the surface is reconstructed by monitoring the amplitude
359 of the oscillating cantilever, which is kept constant by adjusting the z-piezo position through a
360 feedback loop. While scanning in the X-Y direction, the amplitude of the cantilever oscillation is
361 kept constant thanks to a feedback control. However, biomolecules are dynamic in essence;
362 hence, to understand how biomolecules work it was only natural to think about increasing the
363 temporal resolution of conventional AFMs. The first time that the concept of High-Speed (HS)
364 AFM was mentioned -to our knowledge- was in 1991 by Barrett and Quate (Barrett, 1991), who
365 did a fairly attempt with the technology at that time. Other research groups, as Paul Hansma's,
366 would challenge the practical speed limitations. It was only in 2010 when the laboratory leaded
367 by Toshio Ando in Kanazawa University (Japan), filmed individual myosin molecules walking on
368 an actin filament (T Ando et al., 2008), operating their AFM instrument at a speed about 1000
369 times faster than the conventional instruments of that time. Besides the visual impact and
370 scientific insight of those movies, these experiments illustrated that HS-AFM could obtain
371 concomitantly structural and dynamic data, providing insights inaccessible by any other method
372 (Toshio Ando, 2017; Chiaruttini et al., 2015; Kodera et al., 2010; Mierzwa et al., 2017). The basic
373 principles, advantages and limitations of the most common AFM bioimaging mode are nicely
374 detailed in a recent review from Dufrêne *et al.* (Dufrêne et al., 2017).

375 Following the capability of the AFM for mechanical manipulation, to sense and apply small forces
376 accurately (pN-nN range), it rapidly developed into an excellent technique to study interactions
377 -inter and intramolecular forces- at the molecular level, the so-called AFM-based force
378 spectroscopy (AFM-FS). The manipulation of single molecules (single molecule force
379 spectroscopy) has led to fascinating new insights in the mechanics of proteins, polysaccharides,
380 synthetic polymers, and DNA at the molecular level (Florin et al., 1994)(Lee et al.,
381 1994)(Radmacher, 1997)(Noy et al., 1997)(Clausen-Schaumann et al., 2000)(Rief et al.,
382 1997)(Hugel & Seitz, 2001)(P E Marszalek et al., 1999; Piotr E Marszalek et al., 2001)(Giannotti
383 & Vancso, 2007).

384 In the case of lipid bilayers, AFM offers the unique opportunity to probe local physical and
385 mechanical properties, determining the interaction forces with nanoscale lateral resolution,
386 thereby providing new insights into membrane molecular mechanisms. For the nanomechanical
387 characterization with AFM, an SLB is generally first imaged and then a series of force-distance
388 curves is recorded over the same area. In each force-distance curve, the AFM tip away from the
389 surface is approached and retracted at constant velocity while the cantilever deflection is
390 recorded as a function of the Z piezo position. Each portion of the force-distance curve provides
391 information about the physical and mechanical properties of the bilayer, schematized in Figure
392 5. Upon mechanical contact during approach, the cantilever deflection increases and the SLB is
393 elastically compressed by the AFM probe until the tip suddenly breaks through the SLB, jumping
394 into a contact with the substrate (Figure 5, b). The first part of the curve, corresponding to small
395 elastic deformation upon compression, can be used to estimate elastic descriptors of the
396 membrane, like the Young modulus (E), the area compression-expansion modulus (K_A) and
397 bending modulus (k_c) (Dufrêne & Lee, 2000; Picas et al., 2012; L Redondo-Morata et al., 2016).
398 When performing very small elastic deformations (far from the bilayer rupture) it is also often
399 used for this calculation the retraction part of the curve. To estimate the elasticity of the lipid
400 film, the most common model used is the Hertz model, where the surface is approximate to an
401 infinitely half-space of an isotropic elastic solid and the indenter as non-deformable. The
402 parameter describing the sample is the Poisson's ratio (ν), which depends on the nature of the
403 material. For soft biological samples, the Poisson's ratio is generally set to 0.5 (as for
404 incompressible materials). The geometry of the indenter determines the contact area. The
405 original Hertz model considers the shallow contact between two spherical bodies, but several
406 extensions were made for different indenter geometries (D. C. Lin et al., 2007). Again, when
407 performing experiments with small deformations far from the onset of the lipid bilayer rupture,
408 the hysteresis found between the approach and the retract curves is considered as dissipation
409 work and can be used to obtain intrinsic viscoelastic parameters of the viscoelastic material, by
410 the adaptation of common viscoelastic models as power-law rheology or the Kelvin-Voigt model
411 (Garcia et al., 2020).

412 Moreover, different types of short-range interactions can be measured -DLVO, hydration or
413 steric forces-, for further information review here (Lorena Redondo-Morata et al., 2012).



414

415 **Figure 5.** Schematic representation of a representative force curve typically plot in vertical force
 416 vs. tip-sample separation. The red curve represents the tip approaching (a). Right after the
 417 contact area, short-range tip-sample interactions from different nature appear, predominantly
 418 electrostatic (highlighted in pink) and steric (highlighted in green) interactions. When keeping the
 419 tip velocity constant, elastic deformation of the membrane is followed by a sudden jump (b)
 420 which is interpreted as the breakthrough force (F_b) or the maximum force the bilayer is able to
 421 withstand before breaking. F_b has been extensively used as a hallmark of the bilayer stability,
 422 some of these related works are reviewed in this chapter. The AFM tip reaching the hard substrate
 423 underneath is represented as a vertical in the force-separation curve. From the distance in the
 424 curve between the breakthrough force and the substrate it can be estimated the minimal bilayer
 425 thickness (h) (fully compressed). Afterwards, tip retracts at constant velocity (c). Elastic modulus
 426 is usually estimated from the slope of the curve which displays membrane deformation. It is often
 427 observed a hysteresis between the approach and retract curves (yellow area) which is related to
 428 dissipation work and therefore to the viscoelasticity of the material. During retraction, negative
 429 force values are used to estimate the adhesion work between the sample and the AFM tip.
 430 Sometimes, a force plateau when retracting the AFM tip away from the SLB can be observed. It
 431 characterizes a tube pulling process (c'), defined by the tube growing force (F_{tube}) until eventually
 432 the AFM tip completely detaches.

433 The penetration of the AFM tip through the bilayer appears as a discontinuity in the approaching
 434 force-separation curve (Figure 5, b). The vertical force at which this discontinuity happens
 435 corresponds to the maximum force the bilayer is able to stand before breaking and is defined as
 436 the breakthrough force (F_b) or yield threshold force, first observed in the end of the 90's by

437 Dufrêne et al. (Dufrene et al., 1997, 1998)(Dufrêne & Lee, 2000; S Garcia-Manyes & Sanz, 2010;
 438 B. Gumí-Audenis et al., 2016a; L. Redondo-Morata et al., 2012; Schneider et al., 2000). F_b is
 439 generally of several nanonewtons (nN) and it is considered as a direct measurement of the
 440 lateral interactions within the lipid bilayer, at a specified loading rate. From the step in the
 441 separation before and after the breakthrough, the SLB thickness at different compression forces
 442 (and at zero force) can be extracted.

443 The mechanical rupture of lipid bilayers is of thermal fluctuation nature, whose destructive
 444 action is facilitated and directed by the application of the external force. The penetration of the
 445 AFM tip through the SLB has been modeled and conceived as a two-state process with an
 446 associated energy barrier (Butt & Franz, 2002; Franz et al., 2002; Simona Loi et al., 2002).
 447 Specifically, two models describe the activation process. The first is the continuum nucleation
 448 model, which considers the bilayer as a molecular thin homogeneous film -a two-dimensional
 449 fluid layer- between the solid substrate and the solid surface of the AFM tip. The second model
 450 ponders the molecular nature of the lipid bilayer and proposes that each molecule in the SLB
 451 has specific binding sites corresponding to energetically favorable positions. These sites are
 452 energetically equivalent, and as the SLB is pressed by the AFM tip, the energy of the molecules
 453 significantly increases, leading them to jump apart and create a hole under the tip. After a critical
 454 number of molecules have jumped out of the contact area, the tip indents the SLB due to the
 455 high pressure of the remaining molecules, breaking the bilayer. Determining the energy barriers,
 456 represented by the Arrhenius law, governing the lipid membranes rupture process contributes
 457 to the understanding of the extent of the lateral interactions in the bilayer, and this is generally
 458 achieved by following the variation of the F_b with the loading rate (r) by varying the tip-sample
 459 approaching velocity (v) in what is called the dynamic force spectroscopy (DFS). Out of
 460 equilibrium, the F_b increases linearly with the logarithm of r (and of v as well) (Butt & Franz,
 461 2002; S Loi et al., 2002). The loading rate dependence with the thermomechanically activated
 462 nature of the bilayer rupture kinetics leads to the evaluation of the activation energy of the
 463 bilayer failure in the absence of an external force (ΔE_0). The activation energy ΔE for the
 464 formation of a hole in the bilayer that is large enough to initiate rupture and lead the tip
 465 breakthrough can then be calculated following the expression proposed by Butt et al.:

$$\Delta E(F_b) = -k_B \cdot T \cdot \ln \left[\left(\frac{0.693 \cdot k_s}{A} \right) \cdot \frac{dv}{dF_b} \right] \quad (\text{Eq. 1})$$

466 where k_B is the Boltzmann factor, T is the absolute temperature, k_s is the cantilever spring
 467 constant, A is the frequency at which the AFM tip attempts to penetrate the bilayer, generally

468 approximated to the resonance frequency of the cantilever, v is the tip velocity, and F_b the
469 breakthrough force.

470 When retracting the AFM tip away from the SLB, it sometimes remains connected to the bilayer
471 through a lipid tube (Figure 5, d). While the tip moves further away, the membrane tube grows
472 longer until it breaks at a certain distance, and the cantilever returns to the equilibrium position.
473 This tube pulling process occurs at constant force, the tube growing force (F_{tube}) (Armond et al.,
474 2011; Berta Gumí-Audenis et al., 2018; Maeda et al., 2002; Ralf P Richter & Brisson, 2003), and
475 it is observed as a force plateau in the retract part of the force-separation curve (Figure 5), at
476 several tens of pN from which F_{tube} and the tube growing distance (d) can be recorded. Pulling
477 lipid tubes with an AFM tip out of SLBs is a simplified but analogous situation to some biological
478 processes involving mechanical and conformational adjustments -bending, vesiculation,
479 tubulation-like formation of membrane tethers, endocytic vesicles, etc. (Schmidtke & Diamond,
480 2000; Shao et al., 1998; Sheetz, 2001; van Meer et al., 2008). Separation of a membrane segment
481 from the cytoskeleton as well as strong membrane bending are both involved, for which the
482 membrane chemical composition and physicochemical properties are key players. Pulling
483 tethers from cells with an AFM probe is a widely explored approach to evaluate the membrane
484 mechanics on entire cells (Brochard-Wyart et al., 2006; Marcus & Hochmuth, 2002; Nawaz et
485 al., 2015; Sun et al., 2005). Recently, it has also been established as a method to locally probe
486 SLB mechanics and the contribution of the underlying substrate to the measured properties on
487 SLBs (Berta Gumí-Audenis et al., 2018).

488 When pulling tethers from cells, the F_{tube} depends on the membrane properties like bending
489 stiffness (k_c) and in-plane membrane tension (σ), and also on the adhesion between the
490 membrane and the cytoskeleton (Sheetz, 2001). In regions where the membrane has separated
491 from the cytoskeleton -bleb or free membrane-, as there is no direct interaction with the
492 cytoskeleton, F_{tube} strictly relies on k_c and σ (Dai & Sheetz, 1999). However, the cytoskeleton
493 adhesion and σ are difficult terms to separate, and therefore the concept of apparent membrane
494 tension, σ_{app} , has been proposed to include the adhesion energy parameter γ (Sheetz, 2001),
495 $\sigma_{app} = \sigma + \gamma$. When the lipid tube grows under thermodynamic equilibrium, at the limit of zero
496 velocity (static thermodynamic analysis), the following mathematical expression relates the
497 membrane parameters mentioned above with the F_{tube} (Armond et al., 2011; Canham, 1970;
498 Dailant et al., 2005; E Evans & Yeung, 1994; Berta Gumí-Audenis et al., 2018; Hochmuth et al.,
499 1996; Marcus & Hochmuth, 2002; Roux, 2013): $\sigma_{app} = \frac{F_{tube}^2}{8k_c\pi^2}$.

500 The plus of this approach, AFM-based pulling lipid tubes from SLBs, is that it combines the
501 advantage of the AFM local probing with nanoscale lateral and force resolution, with the
502 simplicity of the SLB model preparation. Besides, the local nanomechanical properties of SLBs
503 can be explored through the combination of the tubing force spectroscopy approach and the F_b
504 analysis exposed before, within the same experimental procedure (Berta Gumí-Audenis et al.,
505 2018).

506 Although it will not be extensively discussed here, we find important to mention that the
507 constant force approach can also be used to evaluate the membrane rupture kinetics in SLBs
508 and supported lipid multibilayers (SLMs). The AFM tip is approached at constant velocity, and
509 then compresses the membrane at a constant force (force clamp, FC). Through measuring the
510 time it takes to penetrate the bilayer -time to breakthrough (t_b)- distribution at different
511 compression forces, the AFM-FC mode allows to estimate the rate of bilayer failure and calculate
512 the location of the energy barrier maximum -distance to the transition state- along the reaction
513 coordinate (Δx) and the activation energy (E_0) that characterize the energy barrier (L Redondo-
514 Morata et al., 2012a; Relat-Goberna et al., 2017). Both E_0 as well as Δx were found to be higher
515 for SLBs than for supported lipid multibilayers, endorsing previous suspicion that the mechanical
516 properties of lipid bilayers obtained from nano-indentation are strongly influenced by the
517 underlying hard substrate.

518 4. Phase behavior and nanomechanics. From one component 519 membranes to higher complexity

520 4.1. One-component membranes

521 4.1.1. The gel and the fluid phase

522 To start with the simplest system and increase the complexity in this revision -which does not
523 intend to be exhaustive- consider a one-component phospholipid bilayer, which is thermalized
524 at a temperature far from its T_m , the temperature of the main phase transition, at which a
525 disordering of the hydrophobic tails happens followed by a sudden increase of the lateral
526 mobility. We are then able to distinct two different main phases, gel-like or solid ordered phase
527 (s_o) below T_m , and fluid-like phase or liquid disordered (l_d) above T_m .

528 A mechanical descriptor of lipid bilayers that shows significant differences between both phases
529 is the bending modulus k_c . At $T < T_m$, k_c is an order of magnitude larger than at $T > T_m$, rendering
530 lipid vesicles quite stiff, while softer and more deformable above T_m . In the case of SVLs, where
531 probing deformation is not straightforward, QCM-D has proved to be a useful tool to estimate
532 the extent of vesicle deformation upon adsorption onto surfaces. Reviakine and co-workers

533 (Reviakine et al., 2012) reported deformation measurements of small DMPC vesicles on TiO₂
534 above and below T_m, and experimentally found out that adsorbed vesicle deformation correlates
535 with the bilayer bending modulus. Liposomes in the fluid phase bear a smaller bending modulus
536 and deform to a greater extent.

537 When imaged with the AFM, the SLBs show typically 4-6 nm of height. The measured height is
538 also influenced by both the elasticity of each bilayer and the particular AFM methodology, *i.e.*
539 acoustic-modulation “tapping” mode, contact mode, etc, where the representation of the
540 interface of the lipid bilayer changes. In terms of its mechanical properties, whether we are
541 measuring the elastic deformation or the yield threshold force, a one-component SLB yields a
542 monomodal distribution. While the distribution of deformations or breakthrough forces of the
543 bilayer, being a stochastic process, have been often approached to Gaussian distributions, other
544 distributions based on different theoretical frameworks can also be found in the literature, like
545 the models proposed by Franz *et al.* (Butt & Franz, 2002) for the two-state activation process of
546 the bilayer rupture, mentioned in section 3.2.

547 In the first place, it could be said that, in a general way, the bilayer thickness depends on the
548 nature of the lipids -solid-like bilayers are usually higher than liquid-like counterparts of similar
549 number of carbons in the hydrocarbon chains. In an s₀ phase, the hydrocarbon chains are
550 stretched, so the apparent height is greater, and this is observed when imaging SLBs by AFM.
551 Consequently, stretched acyl chains lead to stronger van der Waals interactions between
552 neighboring molecules, which translates into a shorter intermolecular distance between
553 phospholipids, and a greater mechanical resilience, both elastically and upon AFM tip
554 penetration.

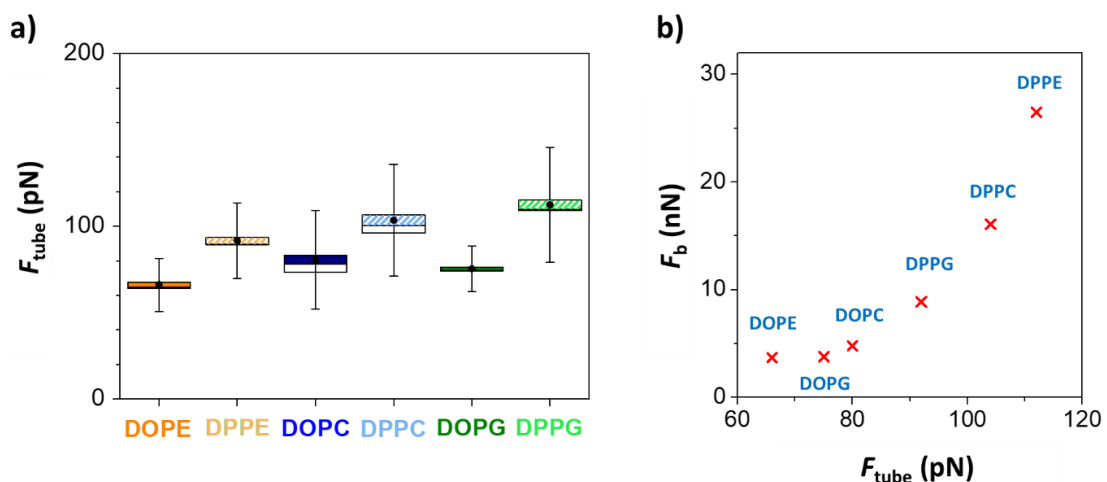
555 For example, let's briefly consider the elastic deformation of DOPC and DPPC, as models of l_d
556 and s₀ SLBs, respectively. The slope of the curve in the contact zone (elastic regime), as we have
557 commented in section 3.2, is related to the elastic modulus of the material. At room
558 temperature, the slope for the DOPC SLB, which is in the fluid phase, is lower than that for the
559 solid DPPC SLB. This indicates that DPPC bears a larger Young modulus than DOPC and thus the
560 membranes in the s₀ phase are therefore stiffer than in the l_d phase. Both slopes are smaller
561 than the one that can be measured on the bare substrate (often assumed as an infinitely stiff
562 material, such as mica).

563 Besides the evidenced difference in elasticity for the fluid and gel-like membranes, l_d SLBs show
564 in general lower F_b values than s₀ SLBs. A good example are homologous series phospholipids;
565 while at room temperature DLPC (T_m ~ -2 °C) SLBs break at force values between 2 and 13 nN,

566 according to the ionic environment, DPPC ($T_m \sim 41.5$ °C) SLBs are pierced by the AFM probe, in
567 similar conditions, in the force range that goes from 7 to 30 nN (Lorena Redondo-Morata et al.,
568 2012). It is also noticeable that the F_b increase with the logarithm of the loading rate is lower for
569 the fluid than for the gel membranes (Lorena Redondo-Morata et al., 2012). This can be
570 expected, if we consider the Bell-Evans or assimilable model, the most likely breaking force
571 depends linearly on the logarithm of the loading rate r , $F(r) = \left(\frac{k_B T}{x}\right) \ln \frac{rx}{K_0 k_B T}$, where k_B is the
572 Boltzmann constant, x is the distance to the transition state and K_0 is the off-rate constant at 0
573 force (E Evans & Ritchie, 1997). In this case, x is directly related to the distance between
574 neighboring phospholipid molecules. This intermolecular distance, therefore x , is smaller in s_o
575 than in l_d .

576 Early work showed how AFM-FS is able to explore quantitatively the molecular determinants
577 that provide mechanical stability to the supported membrane (S Garcia-Manyes, Oncins, et al.,
578 2005a; Sergi Garcia-Manyes et al., 2010). By systematically and independently changing the
579 chemical composition of the lipid headgroup, the length of the hydrophobic tail, and the number
580 of chain unsaturations, {Citation} it was possible to describe the mechanical stability of each
581 bilayer as a direct signature of membrane lateral organization (S Garcia-Manyes et al., 2010).
582 The distribution of F_b values as a function of the length of the hydrophobic chain showed that
583 on average, increasing each hydrocarbon tail by 2 extra $-\text{CH}_2-$ groups results in ~ 7 nN increase
584 of the F_b , equivalent to an enthalpy increase by roughly 2 kJ/mol (Berg et al., 2002). In the same
585 study, the mechanical properties of the linear DPPC were compared with its analogous branched
586 phospholipid, DPhPC, to investigate the effect of acyl chain branching. The distribution of F_b
587 showed a decrease from ~ 20 nN to ~ 12 nN, revealing an important contribution of the lateral -
588 CH_3 groups on the molecular packing of the bilayer. This observation can be rationalized in terms
589 of the larger area per lipid for the branched DPhPC (76.8 \AA^2) compared to that for the linear
590 DPPC (62.0 \AA^2), as revealed by molecular dynamics simulations conducted in the fluid phase
591 (Shinoda et al., 2007). The nanomechanical effect of the $-\text{cis}$ double bonds present in the acyl
592 chains was also investigated. The F_b values distributions for each particular bilayer showed an
593 inversely proportional trend between mechanical stability and number of unsaturations. It was
594 estimated that upon introduction of one additional unsaturation in each acyl chain, F_b values
595 decrease by ~ 5 nN. Interestingly, introducing an asymmetric unsaturation resulted in an even
596 further mechanical destabilization. The resulting molecular tilt reduces the effective packing
597 between molecules, giving rise to a lower T_m (Berg et al., 2002). The findings regarding the
598 mechanical implications of the headgroup chemistry were, however, far less straightforward
599 and highly unanticipated. Comparing phospholipids with the same hydrocarbon tails but

600 different headgroups, a huge range of forces required to indent the bilayer in the same
 601 experimental conditions, spanning from ~ 3 nN (DPPA) all the way up to ~ 66 nN (DPPG).
 602 Furthermore, the lateral packing differences observed between fluid and gel-like bilayers is also
 603 reflected in the tube growing force, pulled as the AFM probe moves away from the SLBs, as this
 604 approach has demonstrated to be sensible to the membrane chemical composition in one-
 605 component SLBs (Maeda et al., 2002)(Berta Gumí-Audenis et al., 2018). Higher F_{tube} values for
 606 DPPC with respect to DMPC have already been observed by Maeda *et al.* (Maeda et al., 2002)
 607 and, as reported in Gumí-Audenis *et al.* (Berta Gumí-Audenis et al., 2018), F_{tube} is lower for l_d
 608 mica-SLBs (in the range of 65–80 pN) than for s_o bilayers of the same headgroup (in the range of
 609 90–110 pN) (Figure 6a). Additionally, while in the l_d state the F_{tube} slightly augments from PE to
 610 PC (66 ± 15 pN for DOPE, 80 ± 25 pN for DOPC and 75 ± 13 pN for DOPG), it clearly increases
 611 when changing the headgroup for s_o membranes from PE to PC and then PG (92 ± 20 pN for
 612 DPPE, 104 ± 30 pN for DPPC and 112 ± 30 pN for DPPG). Hence, F_{tube} is generally higher for s_o
 613 than for l_d and goes along with the lateral packing associated to different phospholipid
 614 headgroups, in a way that is comparable to the trend observed on the F_b approach, as can be
 615 seen in Figure 6b.



616
 617 **Figure 6.** AFM-pulling lipid tubes sensible to the membrane composition in one-component SLBs.
 618 a) F_{tube} values for single component SLBs of different composition (DOPE, DPPE, DOPC, DPPC,
 619 DOPG and DPPG). Boxchart for F_{tube} values show the mean (\bullet), SE (box) and SD (bars). b)
 620 Correlation between F_b and F_{tube} values for single component SLBs. The individual phospholipids
 621 contain a constant tail length of 18 C with 1 unsaturation (DOPE, DOPG and DOPC) or 16 C and
 622 fully saturated (DPPE, DPPC and DPPG), in fluid and gel state at room temperature (RT),
 623 respectively. All the measurements were performed in 150 mM NaCl, 20 mM MgCl_2 , 20 mM

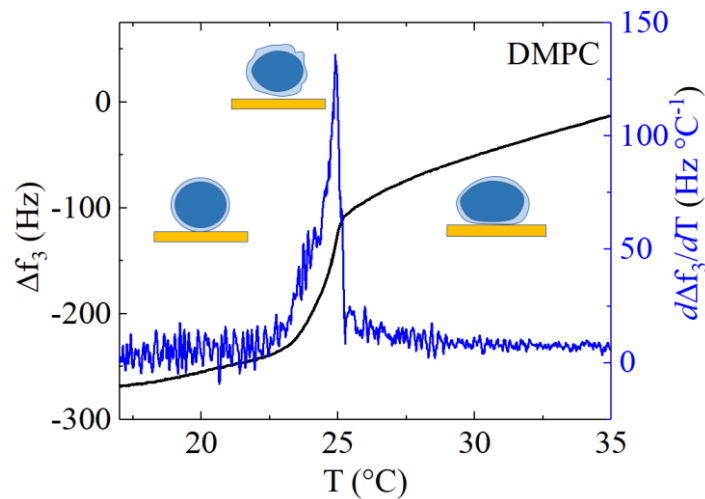
624 HEPES (pH 7.4) buffer solution and at RT. Adapted from Ref. (Berta Gumí-Audenis et al., 2018)
625 with permission from the Royal Society of Chemistry.

626 Taken together, force spectroscopy experiments on SLBs are in qualitative agreement with the
627 literature that correlates the physicochemical properties of membranes with the chemical
628 composition of their phospholipid hydrophobic chains (Rawicz et al., 2000). Noteworthy,
629 thermodynamic quantities such as the melting temperature or the order parameter can be
630 translated into the realm of mechanical stability. The order parameter is usually calculated from
631 NMR-based measurements and provides information about the overall membrane order and
632 more particularly the conformations that the atoms within the lipid tails adopt (Piggot et al.,
633 2017).

634 4.1.2. The thermal transition

635 4.1.2.1. Main transition

636 A useful application of QCM-D is the detection of thermotropic phase transitions within SLBs
637 and SVLs, with the asset that it is label-free, it does not require long temperature equilibration
638 times nor a large amount of sample. When temperature is varied in the absence of any
639 transition, Δf and ΔD typically show a regular, linear temperature dependence, as a reflection of
640 regular, temperature-dependent changes of the viscosity and density of the surrounding liquid
641 medium. When approaching the main phase transition temperature, both frequency and the
642 dissipation responses will differ from a regular temperature dependence, displaying anomalies
643 that reveal that structural changes are taking place (Losada-Pérez et al., 2014; Neupane et al.,
644 2018). Figure 7 displays changes in the frequency and its derivative of an SVL of DMPC of vesicles
645 of around 130 nm, with main transition temperature $T_m \sim 24$ °C in a rather narrow temperature
646 range. The shape of frequency shift curves and its respective temperature derivative are
647 reminiscent of the enthalpy jump and its heat capacity derivative typically obtained from
648 calorimetric measurements (Heimburg, 1998; Losada-Pérez et al., 2014). Dissipation typically
649 shows jumps and minima in the same temperature range. Therefore, extrema in the first-order
650 derivative of frequency and dissipation curves stand as a token of the layer thermotropic phase
651 transitions. Calorimetry is a state-of-the art technique for the detection of phase transitions
652 based on changes in thermal properties when lipids undergo the main (first-order) transition
653 (heat absorption or release), while QCM-D is based on changes in viscoelastic properties of the
654 adsorbed vesicles as a result of changes in bilayer thickness, rigidity and vesicle shape. Although
655 also detectable in SLBs, the size of the jumps in Δf and ΔD is several orders of magnitude smaller
656 than the size of the jumps observed for SVLs (Wargenau & Tufenkji, 2014; Hasan & Mechler,
657 2015).



658

659 **Figure 7.** Temperature dependence of the frequency shift $d\Delta f_3/dT$ (black solid line) and its first-
 660 order derivative (blue solid line) of a DMPC SVL upon heating at 0.2 °C/min.

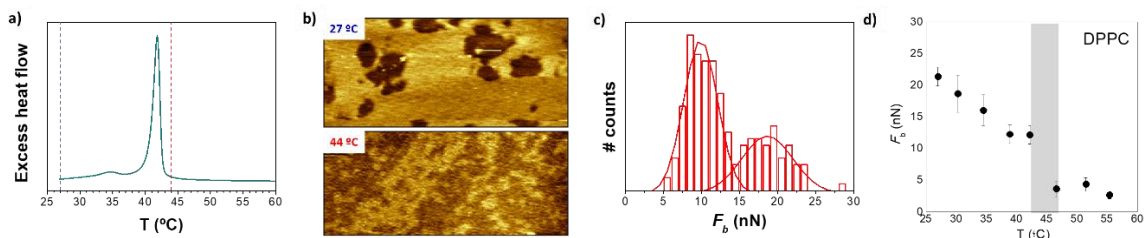
661 Reviakine and coworkers provided a comprehensive interpretation of the mechanisms by which
 662 QCM-D detects phase transitions in lipid membranes and the related relative contribution of
 663 thickness, stiffness and hydrodynamic channels to the Δf and ΔD fingerprints (Peschel et al.,
 664 2016). Upon heating, lipid bilayers in both SVLs and SLBs change from a thicker and stiffer s_o
 665 phase to a thinner and less stiff l_d one. Both stiffness and thickness changes in the lipid layer
 666 properties across the transition encompass changes in the Δf signal (decrease upon heating). In
 667 the case of the ΔD , the stiffness and the thickness contributions oppose each other since stiffer
 668 layers dissipate less. In the SLBs, this leads to an overtone dependence of the transition peak
 669 (Peschel et al., 2016). In thicker and softer SVLs, changes in the shape of the adsorbed vesicles
 670 might induce further hydrodynamic channels that contribute to ΔD . As a consequence, the size
 671 of the maximum in SVLs is several orders of magnitude larger than the one observed in SLBs.

672 The thermotropic phase behavior of pure SLBs has been widely related with the
 673 (nano)mechanical properties of the bilayer. Combining the previously exposed approaches, the
 674 AFM-FS sensitivity to the lipid phase of SLBs is evidenced, positioning it as an appropriate tool
 675 to determine the phase thermal transitions. Temperature controlled-AFM has been established
 676 as a suitable tool to analyze both the topographical and mechanical evolution of biologically
 677 relevant issues that are temperature dependent at the nanometer scale.

678 Seminal work of Leonenko *et al.* demonstrated the existence of several phase transitions in DPPC
 679 and DOPC mica-supported bilayers (Z. V. Leonenko et al., 2004). Data of both topographical
 680 imaging and force measurements provide invaluable insight into membrane behavior during
 681 phase transitions. For DPPC SLBs, F_b values decrease as temperature increases, and beyond the

682 main transition, DPPC shows similar force plots as the fluid-phase DOPC bilayers. This
 683 dependence of the F_b on the phase state of the SLB below and above T_m has been further
 684 reported for different lipids, like DMPC ($T_m \sim 24 \text{ }^\circ\text{C}$) that changes F_b from 13-14 nN at $20 \text{ }^\circ\text{C}$
 685 below T_m to about 6 nN at or $40 \text{ }^\circ\text{C}$ DPPC ($T_m \sim 42 \text{ }^\circ\text{C}$) that shows a switch of F_b from around 20-
 686 25 nN at $27 \text{ }^\circ\text{C}$ to around 3-5 nN at $55 \text{ }^\circ\text{C}$ (S Garcia-Manyes, Guell, et al., 2005; L Redondo-Morata
 687 et al., 2012b). When the DPPC SLB is maintained a temperature slightly above T_m , coexistence
 688 of the gel and fluid phase occurs and a bimodal F_b distribution is obtained (Figure 8), as reported
 689 in Gumí-Audenis *et al.* (B. Gumí-Audenis et al., 2016a). This is because the thermal transitions in
 690 SLBs generally happen at temperatures slightly higher and in a broader range than in vesicle
 691 suspensions as a consequence of the underlying substrate affecting lateral order and interleaflet
 692 coupling (S Garcia-Manyes, Guell, et al., 2005; Z. V Leonenko et al., 2004; L Redondo-Morata et
 693 al., 2012b; Seeger et al., 2010). In Garcia-Manyes *et al.* it was shown that the main phase
 694 transition occurs in a range of temperatures of *ca.* $10\text{-}13 \text{ }^\circ\text{C}$ (S Garcia-Manyes, Oncins, et al.,
 695 2005b).

696 There is an effect of temperature on the mechanical stability for the SLBs because the increase
 697 of temperature directly affects the molecules fluctuations provoking an increment in the area
 698 per molecule -lower packing density-, especially noticeable in the gel phase, with the
 699 consequent decrease of the F_b values. At temperatures around the T_m of the lipid, and for a
 700 temperature range of a few $^\circ\text{C}$, a pronounced drop in F_b takes place, as the SLB gradually
 701 transitions to the fluid phase, thereby softening. Several degrees over the T_m , the F_b values are
 702 on the order of the ones typically observed for l_d SLBs at room temperature (Alessandrini & Facci,
 703 2012; S Garcia-Manyes, Oncins, et al., 2005a; L Redondo-Morata et al., 2012b). This can be seen
 704 in the example shown in Figure 8d, where the DPPC mica-SLB shows an F_b value around of 21
 705 nN at $27 \text{ }^\circ\text{C}$ and slight decreases with temperature as the $42\text{-}45 \text{ }^\circ\text{C}$ range is reached. At higher
 706 temperatures, the F_b remains approximately constant at *ca.* 3.5 nN. The F_b -temperature trend
 707 displays a break around the T_m value of DPPC.



708

709 **Figure 8.** Phase transition of DPPC bilayers: a) DSC thermogram of DPPC vesicle suspension; b) 6
 710 $\mu\text{m} \times 2.5 \mu\text{m}$ AFM images of DPPC silicon-SLB at $27 \text{ }^\circ\text{C}$ and $44 \text{ }^\circ\text{C}$; c) F_b histogram at $44 \text{ }^\circ\text{C}$ and

711 gaussian fits to the bimodal distribution. All experiments performed in 150 mM NaCl, 20 mM
712 MgCl₂, 20 mM HEPES (pH 7.4) buffer solution. Adapted from Ref. (B. Gumí-Audenis et al., 2016a).
713 d) Mean F_b value of DPPC mica-SLB as a function of temperature, in 10 mM HEPES, 20 mM MgCl₂
714 and 150 mM NaCl (pH 7.4). The shadowed vertical line marks the observed transition
715 temperature range. Adapted from Ref. (L Redondo-Morata et al., 2012b)

716 Additionally, Mouritsen and coworkers proposed that AFM topography at a varying temperature
717 could decouple the phase transition of the two different leaflets of the mica-supported bilayer
718 (D. Keller et al., 2005). The low temperature transition was proposed to be related to the melting
719 of the leaflet far from the substrate surface, and the second transition to the phase transition of
720 the leaflet in contact with the mica. Such decoupling would respond to the stronger interaction
721 between the lipid headgroups of the proximal monolayer and the mica support.

722 4.1.2.2. Pretransition

723 Some lipids present a pretransition before the main first-order transition which gives rise to an
724 intermediate order in the lipid bilayers referred to as ripple phase. Ripple phases are curved
725 structures with undulating surface topography. AFM imaging revealed the structure of the ripple
726 phase in hydrated conditions at the nanometer scale (Kaasgaard et al., 2003), and such particular
727 structure has been recently explored nanomechanically (Majewska et al., 2020). It can be found
728 when solid phase lipids experience an increase in temperature and go into the fluid phase, and
729 alternatively it occurs when the fluid phase is cooled down. The observation of this phase
730 transition process is characterized by a melting point temperature of the ripple phase to fluid
731 phase, nucleation point and growth directionality for the formation of the ripple phase. HS-AFM
732 coupled to a temperature-controlled system can report directly ripple to fluid phase transitions
733 (reversibly) in real time and at high resolution (Takahashi et al., 2016). Transition processes from
734 ripple phase to fluid phase and from ripple phase to metastable ripple phase to fluid phase,
735 could be reversibly, phenomenologically and quantitatively studied. In Takahashi *et al.*, results
736 showed phase transition hysteresis in fast cooling and heating processes, while both melting
737 and condensation occurred at 24.15 °C in quasi-steady state situation. A second metastable
738 ripple phase with larger periodicity was formed at the ripple phase to fluid phase transition when
739 the buffer contained Ca²⁺. Thermodynamically, a lipid system containing small domains does not
740 necessarily correspond to a phase coexistence regime, but they may constitute a one phase
741 regime with micro- or nanoscale heterogeneities¹ (Heimburg, 2000). Altogether, these findings

¹ We will further visit this topic in Section 5).

742 may have relevance in more complex cellular systems where lipid nanodomains form and
743 dissociate reversibly.

744 4.2 Phase coexistence

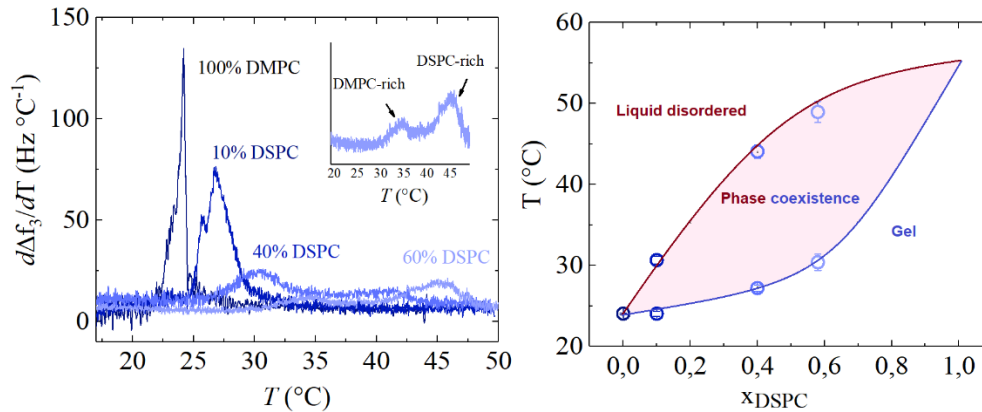
745 Phase segregation and coexistence in lipid bilayers generally happens in the simplest models
746 when mixing a fluid and a gel-like phospholipids, and in the more complex mixtures, like those
747 containing phospholipids, sphingomyelins, ceramides, and cholesterol. At room temperature
748 the bilayers composed of a mixture of a gel and a fluid phospholipid generally segregate into
749 different domains, showing a continuous fluid phase enriched with l_d lipid and thicker dispersed
750 domains associated to a phase enriched in the s_o lipid. When the T_m of the gel-phase lipid is
751 overcome, the binary phospholipid system becomes homogeneous and fluid. Among the many
752 that can be found in the literature, we here mention some examples of these binary systems.

753 The capability of QCM-D to detect lateral phase coexistence and map phase diagrams for binary
754 lipid mixtures of saturated phospholipids will be provided for binary mixtures of homologous
755 phosphatidylcholines DMPC and DSPC, whose chemical structures differ in four methylene
756 groups. This system has been thoroughly investigated experimentally and theoretically in free
757 standing lipid systems (Ehrig et al., 2011; Fidorra et al., 2009; Mabrey & Sturtevant, 1976).
758 DMPC: DSPC mixing behavior is driven by the large hydrophobic mismatch between the two
759 components and departs from ideality as a consequence of the large difference in T_m of the pure
760 constituents.

761 Figure 9 (left panel) shows representative QCM-D signature of phase transitions we now revisit
762 taking place upon heating pure SVLs of pure DMPC and three DMPC: DSPC mixtures (Losada-
763 Pérez, Mertens, et al., 2015). The diameter of the precursor vesicles forming the SVLs was
764 around 130 nm. For pure DMPC, the main transition takes place in a rather narrow temperature
765 range around $T_m \sim 24$ °C. The first-order derivatives of Δf curves capture the typical behaviour
766 of two-component lipid mixtures displaying s_o and l_d phase coexistence. As very low DSPC
767 concentration (DSPC mole fraction = 0.1), the transition is shifted towards higher temperatures
768 and takes place in a broader temperature range indicating a loss of intermolecular cooperation
769 between DMPC molecules to undergo the main transition due to the presence of DSPC. For the
770 mixtures close to the equimolar concentration two small peaks can be observed indicating the
771 coexistence of two phases, s_o and l_d . The peaks are not simple additions of the peaks of the
772 individual constituents, the size of each peak scales with the concentration of each lipid in each
773 coexisting phase. For instance, the inset of Figure 9 displays the peaks of the mixture
774 DMPC: DSPC (40:60). The low-temperature peak corresponds to the DMPC-rich phase, while the

775 high-temperature peak to the DSPC-rich phase. As expected, the size of the latter is higher, since
 776 the concentration of DSPC in the mixture is larger.

777 The analysis of the peaks using the tangent method (Ehrig et al., 2011) to determine the onset
 778 and completion temperatures enables to map the phase diagram of this mixture. The solid lines
 779 are added as a guide to the eye, delimiting the phase coexistence region, dark red (liquidus line),
 780 light blue (solidus line) and follow experimental heat capacity values by Maubrey *et al.* (Mabrey
 781 & Sturtevant, 1976) obtained for multilamellar vesicles of the same concentration.



782

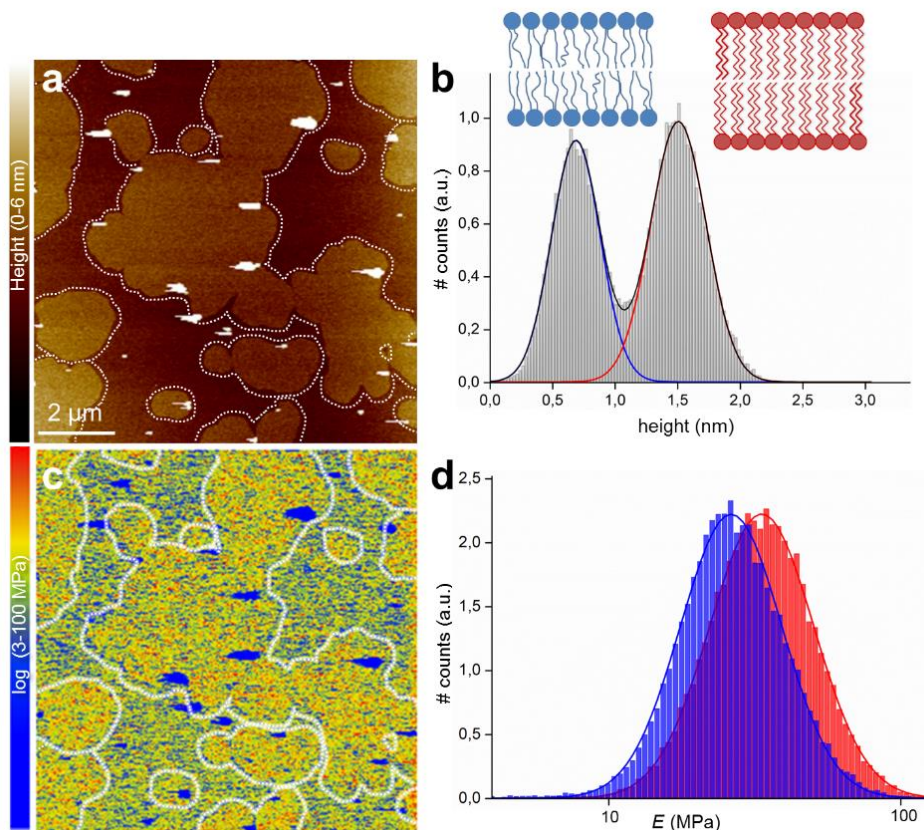
783 **Figure 9.** Left panel: temperature profiles of the first-order temperature derivative of the
 784 frequency shifts for pure DMPC and DMPC:DSPC mixtures 10%, 40% and 60% mole fraction (in
 785 percentage) of DSPC. Right panel: phase diagram obtained from extracting onset and completion
 786 temperatures from the peaks (Losada-Pérez, Mertens, et al., 2015).

787 As discussed in the previous sections, the nanomechanical properties determined by AFM-FS on
 788 SLBs are distinctive of the chemical structure and molecular organization of a bilayer at specific
 789 environmental conditions. This allows for a direct correlation of the elastic modulus, F_b , or F_{tube}
 790 values with the composition in phase-segregated membranes. In most cases, the AFM
 791 topographical characterization easily identifies the segregation of an SLB in different domains,
 792 due to their difference in thickness and compressibility. However, it is possible to reveal the
 793 presence of different domains in an SLB on the basis of their different mechanical properties
 794 even when the domains have a height difference which is too small to be detected by
 795 conventional imaging.

796 Bernchou *et al.* studied, using combined fluorescence microscopy and AFM, the nucleation and
 797 growth of domains in equimolar binary SLBs composed by DOPC and DPPC (Bernchou et al.,
 798 2009), a mixture that shows coexistence of l_d and s_o domains at room temperature (Z. V.
 799 Leonenko et al., 2004). These authors could observe that during cooling the shape of the
 800 domains evolved from compact to a branched morphology, which they discussed as the domain

801 growth being controlled by the diffusion of DPPC from the liquid phase toward the solid domain
 802 interface. In the late stages of the growth, the size and overall shape of the domains depend on
 803 the position of the nucleation points relative to the surrounding nucleation point positions.

804 A mechanical contribution concerning the elastic deformation of the membrane before the
 805 breakthrough point should be considered to fully comprehend the force-distance curve. A
 806 method to study the elastic properties consists of quantitative nanomechanical mapping (Picas
 807 et al., 2012). In (L Redondo-Morata et al., 2016), the equimolar binary lipid mixture DPPC:DOPC
 808 was studied, where l_d and s_o coexisting domains in SLBs are large and directly visually discernable
 809 by AFM imaging (Figure 10a) with clearly distinguishable heights (~ 0.8 nm height difference,
 810 Figure 10b). Elastic modulus nano-mechanical mapping (Figure 10c) shows good agreement
 811 with the E values in the literature, characterized mechanically by AFM (Picas et al., 2012; Rawicz
 812 et al., 2000) and micropipette aspiration (Dieluweit et al., 2010). The mean E values are
 813 26_{-12}^{+58} MPa for the l_d domain and 33_{-15}^{+75} MPa for the s_o domain, respectively (Figure 10d).



814

815 **Figure 10.** PF-QNM AFM Topography and Elasticity mapping of DOPC:DPPC (1:1) SLBs. a)
 816 Topography image (nm) and b) height histogram analysis of the topography (a). The dashed lines
 817 in a) represent the domain edges defined by edge detection. The solid lines in b) are Gaussian fits
 818 to the height distribution, indicating an average height difference between the DOPC l_d (blue line)

819 and DPPC s_o (red line) domains of 0.82 nm. c) The corresponding stiffness map (log scale, MPa)
 820 and d) Young's modulus values histograms (log scale, MPa) of the regions outlined in the
 821 topography (a) and stiffness (c) maps, corresponding to the DOPC (blue) and DPPC (red) domains.
 822 The solid lines are Gaussian fits to the distributions peaking at 26^{+58}_{-12} Mpa (DOPC) and 33^{+75}_{-15} Mpa
 823 (DPPC) (from reference (L Redondo-Morata et al., 2016) with permission).
 824 Using the Young modulus for each domain of the DOPC:DPPC mixture together with the
 825 experimental bilayer thickness (h), the thin shell theory can be used to calculate the area
 826 compression-expansion modulus (K_A) and bending modulus (k_c) as (Rawicz et al., 2000):

$$827 \quad K_A = \frac{Eh}{(1-\nu^2)} \quad \text{and} \quad k_c = \frac{Eh^3}{24(1-\nu^2)}$$

828 When lipid domains separate in lipid mixtures, or when lipids surround membrane embedded
 829 proteins there is, in general, a hydrophobic mismatch at the domain interfaces (Wallace et al.,
 830 2006) or protein/bilayer interfaces (Mouritsen & Bloom, 1984), with an ensuing compression or
 831 stretching of the hydrocarbon chains in the vicinity of the interface. This hydrocarbon tail
 832 stretching or compression may influence the distribution of domain sizes and the kinetics of
 833 domain separation, as well as membrane protein function. The compression/stretching of the
 834 acyl chains of the s_o and l_d domains can be determined by minimizing the elastic energy of the
 835 system, $G_s(x)$, expressed assuming volume conservation (Wallace et al., 2006) as

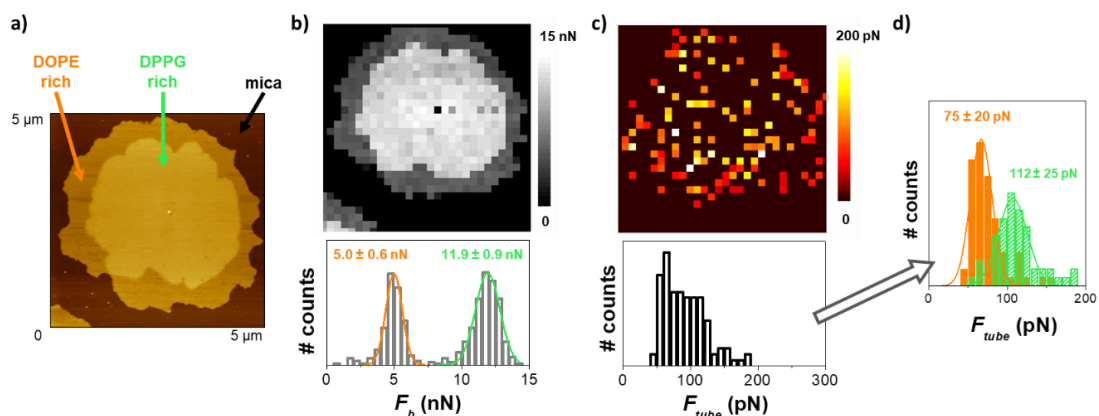
$$836 \quad G_s = \frac{K_o A_o}{2h_o^2} (x - h_o)^2 + \frac{K_d A_d}{2h_d^2} (x - h_d)^2 \quad (2)$$

837 where K_o and K_d are the stretch moduli for s_o and l_d , respectively. A_o and A_d are the lipid area
 838 per molecule for s_o and l_d , respectively. A values are well-documented in literature (notably
 839 through X-ray diffraction and Langmuir methods), being 0.72 nm² for l_d DOPC and 0.49 nm² for
 840 s_o DPPC at room temperature (Nagle & Tristram-Nagle, 2000). h_o and h_d are the measured
 841 bilayer thickness of s_o and l_d , respectively. The estimated G_s values for the DOPC l_d and the DPPC
 842 s_o domains are 0.27 $k_B T$. Hence, the experimental determination of E allows to estimate the
 843 stretch modulus and the bending stiffness of the lipid membrane, as well as the energetic cost
 844 of the lipid domains to accommodate to different thickness.

845 For the SLB system composed of a POPE:POPG mixture (Picas et al., 2009), AFM images revealed
 846 the existence of two separated phases, the higher showing a region with protruding
 847 subdomains. AFM-FS was then used to clarify the nature of each phase. The values of F_b ,
 848 adhesion force and height extracted from the force curves were assigned to the corresponding
 849 s_o (the mechanically stable domains) and l_d phase (the mechanically labile phase). In Crespo-

850 Villanueva *et al.*, while the SLB composed of equimolar DSPC:DOPC was shown to phase
 851 segregate, clearly demonstrated in the AFM topographical images and the correlative F_b maps
 852 and bimodal distributions around ~ 40 nN and ~ 5 nN, the equimolar mixture of the two l_d lipids
 853 DOPC:DOPS led to a homogeneous topography and narrow F_b distribution around 3.5 nN
 854 (Crespo-Villanueva *et al.*, 2018). In Domenech *et al.*, they studied ternary mixtures of
 855 POPC:POPE:CL, a minimum system that mimics the mitochondrial inner membrane (Domenech
 856 *et al.*, 2007). They could observe laterally segregated domains whose height decreased with
 857 increasing temperatures.

858 Pulling lipid tubes with the AFM probe also allows to characterize phase segregated bilayers and
 859 laterally resolve the different domains in multicomponent SLBs (Berta Gumí-Audenis *et al.*,
 860 2018). This is exemplified in Figure 11, a bilayer composed of the l_d lipid DOPE and the s_o lipid
 861 DPPG in ratio DOPE:DPPG 25:75, that at room temperature forms SLB patches with coexisting
 862 domains: gel-phase rich in DPPG, dispersed in fluid-phase rich in DOPE. When indented by the
 863 AFM tip at a constant velocity of $1 \mu\text{m s}^{-1}$, a bimodal F_b distribution is obtained, with
 864 differentiated mean F_b values associated with the fluid (~ 5 nN) and gel (~ 12 nN) domains.
 865 Analyzing the retract force-separation curves that showed the tube pulling event allowed to
 866 represent the F_{tube} distribution and map, where the lower force values (red pixels) are
 867 distributed in the peripheral part of the SLB patch and higher forces (yellow pixels) in the center,
 868 and the F_{tube} distribution is resolved when sorting according to the corresponding F_b , giving a
 869 mean value of 75 ± 20 pN for the DOPE-rich phase, and 112 ± 25 pN for the DPPG-rich phase.
 870 The fact that F_b and F_{tube} for the domains slightly differ from the values for pure DOPE and DPPG
 871 SLBs allows to infer partial miscibility among them.



872

873 **Figure 11.** DOPE:DPPG (25:75). a) AC-mode AFM topographical image; b) F_b map and distribution;874 c) F_{tube} map and distribution; d) F_{tube} distributions resolved by filtering according to the F_b

875 distribution. Reproduced from Ref. (Berta Gumí-Audenis et al., 2018) with permission from the
876 Royal Society of Chemistry.

877 Higher complexity models, like the ternary lipid mixtures containing an unsaturated
878 phosphatidylcholine (PC), a saturated PC or sphingomyelin (SM), and Cholesterol (Chol) have
879 been probably the most studied due to the physiological abundance of these lipids. Depending
880 on the ratio of the components, these mixtures have shown to exhibit two coexisting fluid
881 phases: an l_o phase that is enriched in Chol and SM or saturated PC, and an l_d phase that is
882 predominantly composed of unsaturated PC (Johnston, 2007), and the possibility of a coexisting
883 s_o phase. The group of Schwille has extensively analyzed the domain organization in
884 DOPC/SM/Chol model membranes by means of AFM in combination with fluorescence
885 correlation spectroscopy (FSC) (S Chiantia, Kahya, et al., 2006; S Chiantia, Ries, et al., 2006;
886 Salvatore Chiantia et al., 2007, 2008) and by performing AFM-FS experiments on the different
887 phases they have shown that the average force needed to pierce the l_o phase of the
888 DOPC/SM/Chol bilayer is about 4 nN higher than the one needed to pierce the l_d phase. In a
889 parallel study, Zou and coworkers explored the influence of different cholesterol contents on
890 the morphology and (nano)mechanical stability of phase-segregated DOPC/SM/Chol lipid
891 bilayers by means of AFM imaging and force mapping (R M A Sullan et al., 2010). They observed
892 consistently higher F_b values in the SM/Chol-enriched l_o domains than in the DOPC-enriched l_d
893 phase, and that the (nano)mechanical stability of both coexisting phases counterintuitively
894 decreased with increasing Chol content. By following the dependence of the F_b value with the
895 loading rate in both phases, they calculated the activation energies (ΔE_0) of bilayer rupture at
896 zero applied force. ΔE_0 values obtained were in the range 75-125 kJ/mol for all tested Chol
897 contents and did not show a dependence on the different lipid phases.

898 Besides sphingolipids, ceramides (Cer) have also gained attention in physicochemical studies by
899 means of AFM, since they are known to be predominant in physiologically relevant nanodomains
900 -which have been controversially called for many years lipid rafts (Goñi, 2019a). Longo and
901 coworkers observed that DLPC/GalCer/Chol ternary mixtures only display l_d/s_o coexistence and
902 no l_o phase even at high Chol content (Blanchette et al., 2006). By measuring the area/perimeter
903 ratios of the segregated domains, the authors concluded that Chol was able to decrease the line
904 tension between the two phases. In another study (W.-C. Lin et al., 2007), they could also
905 observe a phase coexistence attributed to l_d/l_o phases with POPC and DOPC at 10 mol% Chol, an
906 indication that fatty acyl chain unsaturation, cholesterol ratio and lipid hydrophobic mismatch
907 in the organization of multi-component lipid systems.

908 Ceramide incorporation on coexisting fluid phase and ordered domains in phase-separated
909 binary and ternary lipid mixtures was shown to affect the lipid spatial organization in domains,
910 with the appearance of a Cer-enriched gel-like phase and the displacement of cholesterol from
911 rafts (S Chiantia, Kahya, et al., 2006; Salvatore Chiantia et al., 2007; Ira et al., 2009). In order to
912 directly probe and quantify the (nano)mechanical stability and rigidity of the Cer-enriched
913 platforms, Zou *et al.* performed AFM topographical images and force mapping that allowed the
914 determination of the F_b value and elastic modulus of the different phases (Ruby May A Sullan et
915 al., 2009a, 2009b; Zou & Johnston, 2010). They confirmed the expulsion of cholesterol from
916 sphingolipid/Chol-enriched domains as a result of Cer incorporation, and observed an increased
917 mechanical stability attributed to the influence of Cer in the lipid organization and packing
918 behavior, also reported later on GalCer rich domains on model membranes with PC and Chol
919 (Berta Gumí-Audenis et al., 2015).

920 The group of Goñi has systematically explored the effect of the acyl compositions of
921 sphingomyelins and the corresponding ceramide counterparts in ternary mixtures with PC and
922 Chol (García-Arribas et al., 2016; González-Ramírez et al., 2019; Jiménez-Rojo et al., 2014)).
923 Combining confocal microscopy, DSC, AFM imaging and FS, they compared the effects of C24:1
924 Cer (nervonoyl ceramide, nCer) with those of C16:0 Cer (palmitoyl ceramide, pCer) in bilayers
925 composed basically of DOPC, SM (either C24:1, nSM or C16:0, pSM) and Chol (García-Arribas et
926 al., 2017). AFM-FS showed that nCer has a lower stiffening effect than pCer, while the presence
927 of nSM reduces the stiffness. When the proportion of phospholipid increases beyond 60 mol %,
928 a lateral phase separation occurs at the micrometer scale (González-Ramírez et al., 2019). The
929 authors interpreted this data as a pCer:Chol interaction, that would predominate at the lower
930 phospholipid concentrations. The putative pCer:Chol complexes (or nanodomains) would mix
931 well with the phospholipid. At higher SM concentrations pSM:pCer and pSM:Chol interactions
932 would become more important, giving rise to the coexisting s_o and l_o phases, respectively.
933 Heterogeneity, or lateral phase separation, occurs more easily with pSM than with DPPC,
934 indicating a higher affinity of SM over DPPC for Chol or Cer. Altogether, the findings of Goñi and
935 coworkers show the sharp increase in complexity when membranes exhibit different
936 sphingolipids of varying N-acyl chains, which should be a common issue in an actual cell
937 membrane environment.

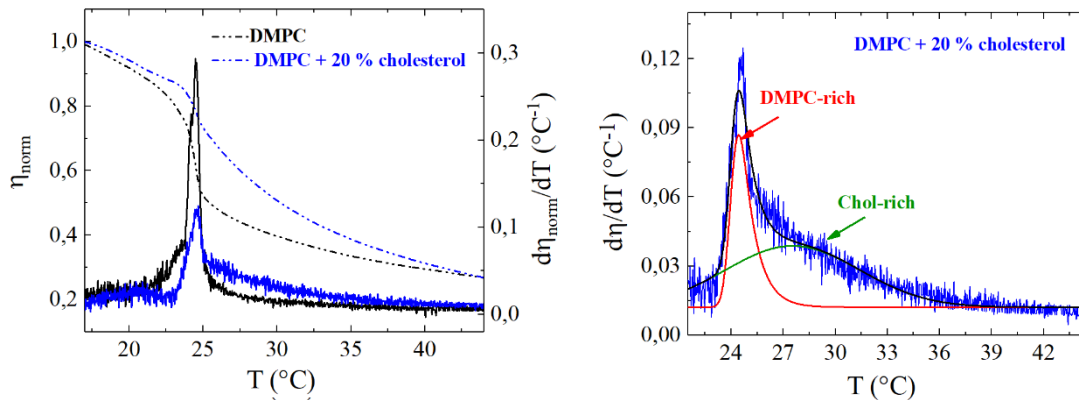
938 1.2. The role of cholesterol

939 Cholesterol is a fundamental constituent of the eukaryotic cell plasma membranes. Eukaryotic
940 cell membranes are not entirely in the conventional l_d phase. Instead, they are, at least partially,
941 in the Chol-rich liquid-ordered (l_o) phase or a phase with similar properties. l_o phase is

942 characterized by a high degree of acyl chain order and is favored by high- T_m lipids with saturated
943 acyl chains such as sphingolipids, when they are mixed with Chol, as exposed in the previous
944 section. Chol plays the essential function of regulating the physical properties of the cell
945 membrane as it controls the lipid organization and phase behavior, regulates the membrane
946 fluidity and its mechanical strength, influencing the passive permeability of water and other
947 small molecules (Pan et al., 2008; Pinkwart et al., 2019). From the molecular perspective, Chol
948 is considered to produce a condensing effect and induce ordering to fluid phase lipids forming
949 the membrane and to have the opposite effect on phospholipids present in the gel phase (Hung
950 et al., 2007; Rog et al., 2009). However, several experiments pointed out the complex effect of
951 Chol on lipid bilayers, which depends on the molecular structure of the neighboring lipids: the
952 degree of chain unsaturation, the length of the hydrophobic tail and the chemistry of the
953 headgroup (Pan et al., 2008; Mills et al., 2009; Garcia-Manyes et al., 2010). In view of
954 acknowledging the particular role of cholesterol, let us briefly outline results on the phase
955 behavior of SVLs and SLBs consisting of binary mixtures of saturated phospholipids and
956 cholesterol using mechanical descriptors such as shear viscosity of SVLs and nanomechanics of
957 SLBs.

958 We first describe the phase behavior of SVLs containing binary mixtures of DMPC:Chol using
959 QCM-D. Upon the addition of Chol to phospholipid bilayers, the sharp main phase transition in
960 pure DMPC gradually diminishes and eventually disappears over a given Chol concentration. In
961 the case of DMPC, SVLs showed no transition from 30% cholesterol. Figure 12 shows normalized
962 shear viscosity $\eta_{norm} = [\eta(t)/\eta(t=0)]$, with t the time] for pure DMPC and DMPC:Chol (20 mol %
963 Chol) calculated using a Voigt-based viscoelastic model (Voinova et al., 1999). At intermediate
964 Chol concentrations, asymmetric peaks can be observed. These peaks encompass two main
965 contributions, a sharp, narrow peak and a broader one that overlaps with the former (see right
966 panel in Figure 12 for a more detailed view including Gaussian fitting). Two domains can be
967 identified, namely, the sharp contribution can be ascribed to the pure DMPC-rich domains
968 undergoing the main transition and the latter to the Chol-rich ones. The broader peak appears
969 as a result of the reduced mobility of the hydrophobic chains of DMPC in Chol-rich domains. The
970 presence and the size of these domains depend strongly on the concentration of cholesterol and
971 the temperature. On increasing the amount of cholesterol, the temperature range of the overall
972 transition increases as a result of the extension of the second broad contribution, while the size
973 of the maximum corresponding to the melting of the single lipid decreases. No phase transition
974 is detected at Chol concentration over 30 mol % indicating the formation of a homogeneous
975 liquid ordered l_o phase at a macroscopic level. Such a large cholesterol concentration inhibits

976 the formation of extended domains. A similar pattern of behavior was observed for DPPC:Chol
 977 SVLs, however, for this later system, the completion temperature of the overall transition at
 978 intermediate cholesterol concentrations was not attained, due to the (upper) limited
 979 temperature range of commercial QCM-D systems (Losada-Pérez, Khorshid, et al., 2015). These
 980 results are in agreement with recent calorimetric studies of free-standing membranes of the
 981 same systems (Mannock et al., 2010).

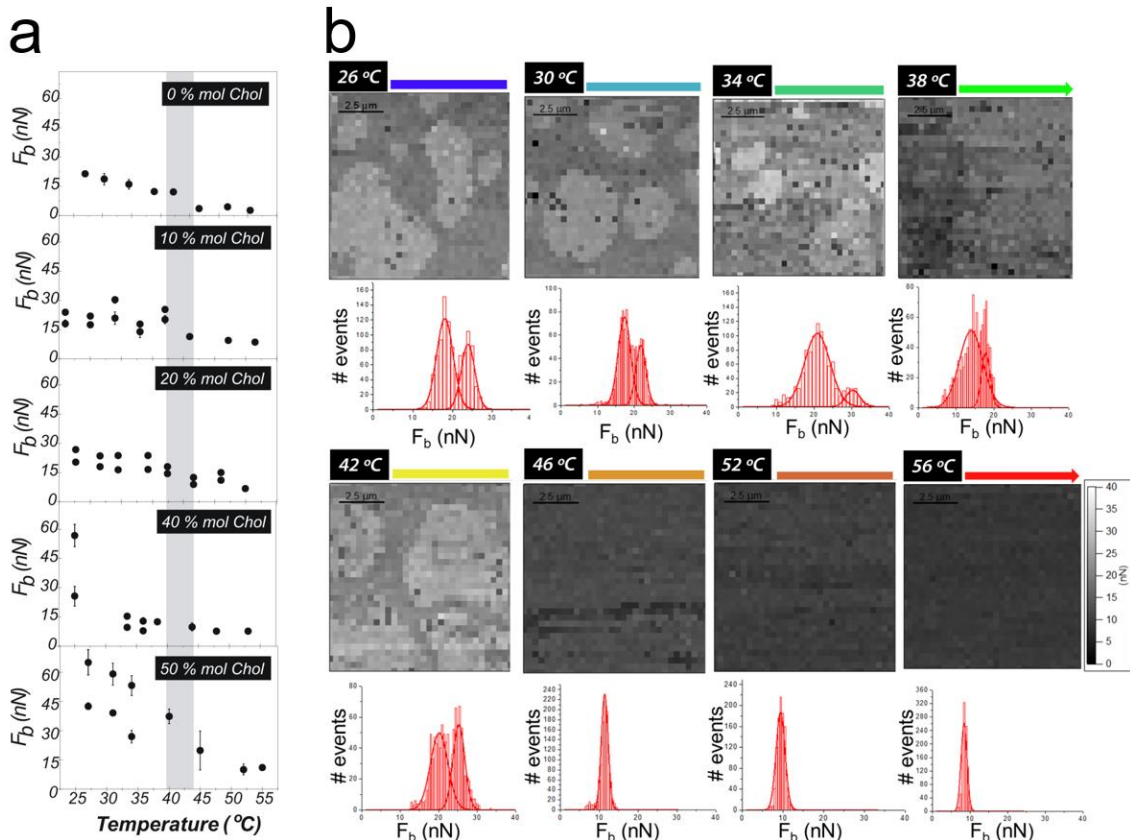


982
 983 **Figure 12.** Left panel Temperature dependence of the normalized effective shear viscosity (dash
 984 dotted lines) and its first-order derivative (solid line) of DMPC and DMPC + 20% cholesterol SVLs
 985 on a supported vesicle layer on a gold-coated QCM-D quartz sensor upon heating. Right panel
 986 closer view of the normalized shear viscosity first-order derivative for DMPC + 20% cholesterol
 987 SVLs. Solid lines denote multiple peak gaussian fitting.

988 The role of Chol in the structure and nanomechanics of SLBs has been extensively studied by
 989 AFM (L Redondo-Morata et al., 2012b; R M A Sullan et al., 2010; Al-Rekabi & Contera, 2018; S
 990 Garcia-Manyes et al., 2010; Adhyapak et al., 2018), as well as its interplay with sphingolipids or
 991 other lipids (García-Arribas et al., 2016; 2006; Ahyayauch et al., 2002; Guyomarc'h et al., 2014)
 992 and further reviewed in (B. Gumí-Audenis et al., 2016b).

993 By means of temperature-controlled AFM imaging and AFM-FS to assess the influence of Chol
 994 on the membrane ordering and stability (Redondo-Morata et al., 2012), this work analyzed a
 995 DPPC:Chol in representative range of compositions up to 50 mol % Chol, studying the phase
 996 evolution upon heating (from room temperature to temperatures high above the T_m of DPPC)
 997 and the corresponding (nano)mechanical stability. This provided a correlation between the
 998 mechanical behavior and composition with the lateral order of each phase present in the
 999 bilayers. It proved that low Chol contents lead to a phase segregated system, while high contents
 1000 of Chol can give a homogeneous topography, although a bimodal F_b distribution was observed,
 1001 possibly due to the presence of small heterogeneities that could not be resolved in the images.
 1002 In all cases, it was demonstrated that Chol enhances the mechanical stability of the binary

1003 membrane, and an extraordinarily stable system was observed for equimolar fractions (50 mol
1004 % Chol). In addition, even when no thermal transition was detected by the traditional bulk
1005 analysis techniques for vesicles with high Chol content (40 and 50 mol %), it was shown that
1006 temperature-controlled AFM-FS is capable of identifying a thermal transition for the SLBs. As
1007 detailed in Figure 13, for high-Chol contents -40 and 50 mol %- the DPPC:Chol system shows a
1008 double F_b distribution at room temperature, probably due to the presence of (space or time)
1009 non-resolved heterogeneities for these compositions. Although no thermal transition was
1010 observed in DSC thermograms of free-standing systems, when AFM-FS experiments were
1011 performed at different temperatures for these systems, a gradual decrease of the mean F_b value
1012 was observed until temperature reached ca. 40 °C. The continuous decrease in the F_b value with
1013 increasing temperature may be ascribed to an increase in fluidity of the system, and it is evident
1014 that, although not detected in DSC of DPPC:Chol vesicles, a transition occurs for DPPC:Chol SLBs
1015 with 40 and 50 mol % Chol around 42-45 °C. Below this temperature, the system in the l_o phase
1016 presents extraordinary lateral order and may have properties that resemble a gel-like bilayer,
1017 and as temperature increases, it gradually becomes a system with higher lateral mobility (but
1018 still with higher order than the DPPC l_d phase). This behavior indicates that for DPPC:Chol SLBs,
1019 a thermal transition occurs even for high-Chol compositions, in a temperature range between
1020 ca. 42-47 °C independently of the membrane composition, and that it may probably be of
1021 second-order for the high-Chol DPPC:Chol bilayers (40-50 mol %), which generally appear as a
1022 very broad transition or it is even not detected in DSC experiments of free standing vesicles or
1023 QCM-D of SVLs.



1024

1025 **Figure 13.** a) Mean F_b value of DPPC:Chol SLBs in 10 mM HEPES, 20 mM MgCl_2 and 150 mM NaCl,
 1026 pH 7.4, with various Chol contents, as a function of temperature. The shadowed vertical line
 1027 marks the temperature range where the main transition in pure DPPC occurs. For DPPC:Chol SLBs
 1028 with 40 and 50 mol % Chol, although not detected in DSC of DPPC:Chol vesicles, a transition occurs
 1029 around 42–45 $^{\circ}\text{C}$. b) F_b maps and distributions for DPPC:Chol SPB with 10 mol % Chol, in 10 mM
 1030 HEPES, 20 mM MgCl_2 and 150 mM NaCl, pH 7.4, with increasing temperature. Reprinted from (L
 1031 Redondo-Morata et al., 2012b).

1032 Strikingly, information about the lateral in-plane structure of such systems can be instead
 1033 obtained by grazing incidence XR diffraction (GIXD). In (Gumi-Audenis et al., 2018), a silicon-SLB
 1034 system was designed in order to deal with the requirement of the wetting preservation to
 1035 guarantee the membrane stability while minimizing the background from the liquid
 1036 environment. Using this methodology, it was confirmed that DPPC:Chol with low contents of
 1037 Chol up to 30 mol % lead to separation into two coexisting phases at room temperature and
 1038 concentrations higher than 30 mol % Chol appear to be a unique l_o phase. This condition was
 1039 consistent with the earlier work (Redondo-Morata et al., 2012b) demonstrating that such
 1040 increase of nanomechanical resistance is associated to a strong lateral interaction mediated by
 1041 Chol molecules placed between the DPPC ones, due to a highly stable structure with most
 1042 probably an equimolar DPPC:Chol ratio.

1043 To date, efforts continue to understand the complex role of cholesterol in biomembranes. Still,
1044 these discoveries cannot always be directly translated to the behavior of living cell membranes.
1045 By means of advanced fluorescence imaging and spectroscopy, Sezgin and colleagues (Pinkwart
1046 et al., 2019) have shown that cholesterol diffuses faster than phospholipids in live membranes,
1047 but not in model membranes. Interestingly, a detailed statistical diffusion analysis suggested
1048 two-component diffusion for cholesterol in the plasma membrane of live cells.

1049 Recent work based on a systematic AFM-FS study on DOPC:Chol SLBs at varying ratios suggested,
1050 however, that cholesterol may not just be responsible of increasing the mechanical stability but
1051 also introduce irregularities across the leaflets (Adhyapak et al., 2018). At Chol ratios above 20%,
1052 they could observe two sudden jumps in the force-distance curve, the second jump always
1053 displaying shorten separation. They interpreted that cholesterol induced asymmetry across the
1054 (in the inner and outer leaflets) bilayer, related to the phenomena of interleaflet coupling and
1055 depending on Chol concentration.

1056 Recently, Contera and coworkers took a different approach to study the effect of Chol in the
1057 mechanical properties of lipid bilayers (Al-Rekabi & Contera, 2018). Applying different
1058 frequencies simultaneously in an AFM topography mode, namely amplitude modulation–
1059 frequency modulation (AM–FM), they investigated the effect of Chol on DPPC bilayers in
1060 concentrations from 0 to 60 %. The lipid bilayers probed with this methodology displayed both
1061 elastic and viscous behavior. Cholesterol showed to modulates both, increasing elastic and
1062 viscous components as a function of Chol concentrations. The authors interpreted that their
1063 results may have a physiological relevance, where such viscoelastic properties may be used by
1064 cells to modulate the propagation (elastic) or attenuation (viscous) of mechanical signals across
1065 the cell membrane.

1066 5. Connection between nanoscale measurements and 1067 thermodynamic descriptors of membranes

1068

1069 When studying phase coexistence in lipid membranes a distinction between thermodynamically
1070 stable phases and transient local domains in lipid bilayer at equilibrium should be made. Let us
1071 briefly discuss this in line with the above-exposed results on phospholipid-cholesterol binary
1072 mixtures. PC-Chol binary mixtures have been studied for many years using a plethora of
1073 experimental techniques. Yet, despite their apparent simplicity being two-component systems,
1074 their phase behavior remains controversial and, in many cases, departs from the canonical phase
1075 diagram proposed by Vist and Davis (Vist & Davis, 1990). In fact, results depend strongly on the

1076 spatio-temporal resolution of the different experimental techniques. For instance, unlike
1077 predicted by most phase diagrams, l_d - l_o phase coexistence was not observed for micron-sized
1078 GUVs of DPPC-cholesterol mixtures using fluorescence microscopy (Veatch & Keller, 2003),
1079 while some other techniques captured this phenomenon for free standing MLVs vesicles (DSC
1080 (Mannock et al., 2010), volumetric (Miyoshi et al., 2014), NMR (Davis et al., 2009), SLBs (AFM)(L
1081 Redondo-Morata et al., 2012b), and SVLs (QCM-D)(Losada-Pérez, Khorshid, et al., 2015). These
1082 findings suggest that, instead of macroscopic phase separation, these systems are presumably
1083 filled with mesoscopic and nanoscopic domains, whose size and lifetime depends on
1084 temperature and mixture composition (Winkler et al., 2017).

1085 Classically, when dealing with phase separation the Gibbs' phase rule is customarily invoked,
1086 assuming macroscopic phase coexistence and neglecting the role of phase boundaries, which
1087 comparably, hardly contribute to the free energy. If domains are small, the interfaces between
1088 domains constitute an important part of the system and its contribution to the free energy is
1089 not negligible. In this respect, using the term phase in the classical thermodynamic sense might
1090 not be appropriate (Heimburg, 1998; Almeida et al., 2005). Following Hill (Hill, 2013) a system
1091 can no longer be called a phase when it ceases to behave like a macroscopic system and starts
1092 behaving like a small system.

1093 In this respect, both AFM and QCM-D have demonstrated to be valuable tools to detect domain
1094 (nano/mesoscopic sized domains) coexistence within supported membranes of binary lipid
1095 mixtures.

1096 6. Conclusions and future perspectives

1097 As mentioned in the previous sections, AFM-FS can interestingly resolve coexistence of domains
1098 at concentrations where height differences at domain boundaries are not detectable.
1099 Breakthrough force thus stands as a useful mechanical descriptor to resolve domain coexistence.
1100 Even though domains cannot be considered as phases in the purely thermodynamic standpoint,
1101 this does not mean that these systems cannot be treated in a rigorous thermodynamic way. As
1102 a matter of fact, the breakthrough force is able to detect a thermal transition at high cholesterol
1103 concentrations in binary PC:Chol SLBs, whose origin deserves to be revisited and further
1104 explored in the framework of either fluctuations arising in the vicinity of a critical point, the
1105 possibility of glassy-cholesterol-rich nanodomains or eventual cholesterol crystallization. In this
1106 sense, the development of HS-AFM will likely provide new insights due to its unprecedented
1107 spatio-temporal resolution, thanks to a direct correlation between structure and diffusion
1108 (Munguira et al., 2016). Similarly, HS Force Spectroscopy has the capacity to cover a wider force

1109 spectrum, which can help to validate theoretical frameworks of the field, as well as provide a
1110 direct correlation with Molecular Dynamics simulations (Rico et al., 2013).

1111 There is indeed plenty of room in fundamental lipid biophysics and phase behavior in particular
1112 to use both purely mechanical and viscoelastic properties as descriptors to provide a more
1113 complete picture of the origins of domain formation and coexistence. The ultimate lipid phase
1114 coexistence to be fully understood are transient nanodomains, often (confusively) referred to
1115 as lipid rafts. There is to date no agreement about the size and lifetime of rafts, and the term is
1116 used to referred to a collection of different structures (Goñi, 2019). Based on the current
1117 knowledge, microdomains in equilibrium are no longer considered suitable models for the
1118 biological structure that rafts represent. Fortunately, advanced super-resolution microscopies
1119 and fast techniques are becoming available and will shed some light in one of the most discussed
1120 topics in biomembrane studies.

1121 In light of this, multiscale spatio-temporal measurements of mechanical properties of supported
1122 membranes can help to experimentally address different scenarios where membrane micro- and
1123 nano-domain formation finds theoretical support. Starting from equilibrium ternary lipid
1124 mixtures in the vicinity of a critical point, it might be worth exploring how the presence of critical
1125 fluctuations reflects in the membrane mechanical properties, and if these properties can be
1126 used as physical descriptors to test critical-point universality laws. Secondly, tuning membrane
1127 (local and global) environment by actively controlling curvature, leaflet asymmetry, solid
1128 support topography and addition of external components would help complete the manifold
1129 where domain formation occurs. Finally, the growing spatiotemporal capabilities of AFM are
1130 promising tools to explore membrane organization in the realm of non-equilibrium phenomena.

1131 7. Acknowledgements

1132 We acknowledge financial support from the Generalitat de Catalunya (2017-SGR-1442), the
1133 Instituto de Salud Carlos III, through “Acciones CIBER” and CIBER-BBN FlexQS-skin and FelxCAB
1134 projects. This work was also supported by a grant overseen by the French National Research
1135 Agency (ANR) as part of the “Investments d’Avenir” Programme (I-SITE ULNE / ANR-16-IDEX-
1136 0004 ULNE) to L.R.-M. Financial support from the project ‘SADI’ by the programme Action
1137 Recherche Concertée, Université Libre de Bruxelles (ULB) to P.L-P is also acknowledged.

1138 8. Glossary of lipid acronyms

1139

Acronym	Long name
---------	-----------

<i>C16:0 palmitoyl Cer (aka palmitoyl Cer, pCer)</i>	N-palmitoyl-D-erythro-sphingosine
<i>C16:0 palmitoyl SM (aka palmitoyl SM)</i>	N-palmitoyl-D-erythro-sphingosylphosphorylcholine
<i>C24:1 nervonoyl Cer (aka nervonoyl Cer, nCer)</i>	N-nervonoyl-D-erythro-sphingosine
<i>C24:1 nervonoyl SM (aka nervonoyl SM)</i>	N-Nervonoyl-D-erythro-sphingosylphosphorylcholine-d9
<i>Cer</i>	ceramide
<i>Chol</i>	cholesterol
<i>CL</i>	cardiolipin
<i>DMPC</i>	1,2-dimyristoyl-sn-glycero-3-phosphocholine
<i>DOPC</i>	1,2-dioleoyl-sn-glycero-3-phosphocholine
<i>DOPE</i>	1,2-dioleoyl-sn-glycero-3-phosphoethanolamine
<i>DOPG</i>	1,2-dioleoyl-sn-glycero-3-[phospho-rac-(3-lysyl(1-glycerol))]
<i>DOTAP</i>	1,2-dioleoyl-3-trimethylammonium-propane
<i>DPPA</i>	1,2-dipalmitoyl-sn-glycero-3-phosphate
<i>DPPC</i>	1,2-dipalmitoyl-sn-glycero-3-phosphocholine
<i>DPPE</i>	1,2-dipalmitoyl-sn-glycero-3-phosphoethanolamine
<i>DPPG</i>	1,2-dipalmitoyl-sn-glycero-3-phospho-(1'-rac-glycerol)
<i>DSPC</i>	1,2-distearoyl-sn-glycero-3-phosphocholine
<i>GalCer</i>	Galactosylceramides
<i>PC</i>	phosphocholine
<i>PE</i>	phosphoethanolamine
<i>POPC</i>	1-palmitoyl-2-oleoyl-glycero-3-phosphocholine
<i>POPE</i>	1-palmitoyl-2-oleoyl-sn-glycero-3-phosphoethanolamine
<i>POPG</i>	1-palmitoyl-2-oleoyl-sn-glycero-3-phospho-(1'-rac-glycerol)
<i>SM</i>	sphingomyelin

9. References

1140

1141

1142 Adhyapak, P. R., Panchal, S. V., & Murthy, A. V. R. (2018). Cholesterol induced asymmetry in

1143 DOPC bilayers probed by AFM force spectroscopy. *Biochimica et Biophysica Acta (BBA)*1144 - *Biomembranes*, 1860(5), 953–959. <https://doi.org/10.1016/j.bbamem.2018.01.021>

1145 Ahyayauch, H., Requero, M. A., Alonso, A., Bennouna, M., & Goni, F. M. (2002). Surfactant

1146 effects of chlorpromazine and imipramine on lipid bilayers containing sphingomyelin

1147 and cholesterol. *Journal of Colloid and Interface Science*, 256(2), 284–289.1148 <https://doi.org/10.1006/jcis.2002.8690>

- 1149 Alessandrini, A., & Facci, P. (2012). Nanoscale mechanical properties of lipid bilayers and their
1150 relevance in biomembrane organization and function. *Micron*, 43(12), 1212–1223.
1151 <https://doi.org/10.1016/j.micron.2012.03.013>
- 1152 Almeida, P. F. F., Pokorny, A., & Hinderliter, A. (2005). Thermodynamics of membrane
1153 domains. *Biochimica et Biophysica Acta (BBA) - Biomembranes*, 1720(1), 1–13.
1154 <https://doi.org/10.1016/j.bbamem.2005.12.004>
- 1155 Al-Rekabi, Z., & Contera, S. (2018). Multifrequency AFM reveals lipid membrane mechanical
1156 properties and the effect of cholesterol in modulating viscoelasticity. *Proceedings of*
1157 *the National Academy of Sciences*, 115(11), 2658–2663.
1158 <https://doi.org/10.1073/pnas.1719065115>
- 1159 Ando, T, Uchihashi, T., Kodera, N., Yamamoto, D., Miyagi, A., Taniguchi, M., & Yamashita, H.
1160 (2008). High-speed AFM and nano-visualization of biomolecular processes. *Pflugers*
1161 *Archiv-European Journal of Physiology*, 456(1), 211–225.
1162 <https://doi.org/10.1007/s00424-007-0406-0>
- 1163 Ando, Toshio. (2017). High-speed atomic force microscopy and its future prospects. *Biophysical*
1164 *Reviews*, 10(2), 285–292. <https://doi.org/10.1007/s12551-017-0356-5>
- 1165 Armond, J. W., Macpherson, J. V., & Turner, M. S. (2011). Pulling Nanotubes from Supported
1166 Bilayers. *Langmuir*, 27(13), 8269–8274.
- 1167 Bangham, A. D., & Horne, R. W. (1964). Negative staining of phospholipids and their structural
1168 modification by surface-active agents as observed in the electron microscope. *Journal*
1169 *of Molecular Biology*, 8(5), 660-IN10. [https://doi.org/10.1016/S0022-2836\(64\)80115-7](https://doi.org/10.1016/S0022-2836(64)80115-7)
- 1170 BANGHAM, A. D., PETHICA, B. A., & SEAMAN, G. V. (1958). The charged groups at the interface
1171 of some blood cells. *The Biochemical Journal*, 69(1), 12–19.
1172 <https://doi.org/10.1042/bj0690012>

- 1173 Barrett, R. C. (1991). High-speed, large-scale imaging with the atomic force microscope.
1174 *Journal of Vacuum Science & Technology B: Microelectronics and Nanometer*
1175 *Structures*, 9(2), 302. <https://doi.org/10.1116/1.585610>
- 1176 Berg, J. M., Tymoczko, J. L., Stryer, L., Berg, J. M., Tymoczko, J. L., & Stryer, L. (2002).
1177 *Biochemistry* (5th ed.). W H Freeman.
- 1178 Bernchou, U., Ipsen, J. H., & Simonsen, A. C. (2009). Growth of solid domains in model
1179 membranes: Quantitative image analysis reveals a strong correlation between domain
1180 shape and spatial position. *The Journal of Physical Chemistry. B*, 113(20), 7170–7177.
1181 <https://doi.org/10.1021/jp809989t>
- 1182 Binnig, G., Quate, C. F., & Gerber, C. (1986). ATOMIC FORCE MICROSCOPE. *Physical Review*
1183 *Letters*, 56(9), 930–933. <https://doi.org/10.1103/PhysRevLett.56.930>
- 1184 Blanchette, C. D., Lin, W.-C., Ratto, T. V., & Longo, M. L. (2006). Galactosylceramide Domain
1185 Microstructure: Impact of Cholesterol and Nucleation/Growth Conditions. *Biophysical*
1186 *Journal*, 90(12), 4466–4478. <https://doi.org/10.1529/biophysj.105.072744>
- 1187 Brochard-Wyart, F., Borghi, N., Cuvelier, D., & Nassoy, P. (2006). Hydrodynamic narrowing of
1188 tubes extruded from cells. *Proceedings of the National Academy of Sciences*, 103(20),
1189 7660.
- 1190 Butt, H. J., & Franz, V. (2002). Rupture of molecular thin films observed in atomic force
1191 microscopy. I. Theory. *Physical Review E*, 66(3).
1192 <https://doi.org/10.1103/PhysRevE.66.031601>
- 1193 Canham, P. B. (1970). The minimum energy of bending as a possible explanation of the
1194 biconcave shape of the human red blood cell. *Journal of Theoretical Biology*, 26(1), 61–
1195 81.
- 1196 Chiantia, S, Kahya, N., Ries, J., & Schwille, P. (2006). Effects of ceramide on liquid-ordered
1197 domains investigated by simultaneous AFM and FCS. *Biophysical Journal*, 90(12),
1198 4500–4508. <https://doi.org/10.1529/biophysj.106.081026>

- 1199 Chiantia, S, Ries, J., Kahya, N., & Schwille, P. (2006). Combined AFM and two-focus SFCS study
1200 of raft-exhibiting model membranes. *Chemphyschem*, 7(11), 2409–2418.
1201 <https://doi.org/10.1002/cphc.200600464>
- 1202 Chiantia, Salvatore, Kahya, N., & Schwille, P. (2007). Raft domain reorganization driven by
1203 short- and long-chain ceramide: A combined AFM and FCS study. *Langmuir*, 23(14),
1204 7659–7665. <https://doi.org/10.1021/la7010919>
- 1205 Chiantia, Salvatore, Ries, J., Chwastek, G., Carrer, D., Li, Z., Bittman, R., & Schwille, P. (2008).
1206 Role of ceramide in membrane protein organization investigated by combined AFM
1207 and FCS. *Biochimica Et Biophysica Acta-Biomembranes*, 1778(5), 1356–1364.
1208 <https://doi.org/10.1016/j.bbamem.2008.02.008>
- 1209 Chiaruttini, N., Redondo-Morata, L., Colom, A., Humbert, F., Lenz, M., Scheuring, S., & Roux, A.
1210 (2015). Relaxation of Loaded ESCRT-III Spiral Springs Drives Membrane Deformation.
1211 *Cell*, 163(4), 866–879. <https://doi.org/10.1016/j.cell.2015.10.017>
- 1212 Cho, N.-J., Frank, C. W., Kasemo, B., & Höök, F. (2010). Quartz crystal microbalance with
1213 dissipation monitoring of supported lipid bilayers on various substrates. *Nature*
1214 *Protocols*, 5(6), 1096–1106. <https://doi.org/10.1038/nprot.2010.65>
- 1215 Cho, N.-J., Kanazawa, K. K., Glenn, J. S., & Frank, C. W. (2007). Employing Two Different Quartz
1216 Crystal Microbalance Models To Study Changes in Viscoelastic Behavior upon
1217 Transformation of Lipid Vesicles to a Bilayer on a Gold Surface. *Analytical Chemistry*,
1218 79(18), 7027–7035. <https://doi.org/10.1021/ac0709504>
- 1219 Choi, S.-E., Greben, K., Wördenweber, R., & Offenhäusser, A. (2016). Positively charged
1220 supported lipid bilayer formation on gold surfaces for neuronal cell culture.
1221 *Biointerphases*, 11(2), 21003. <https://doi.org/10.1116/1.4945306>
- 1222 Clausen-Schaumann, H., Rief, M., Tolksdorf, C., & Gaub, H. E. (2000). Mechanical stability of
1223 single DNA molecules. *Biophysical Journal*, 78(4), 1997–2007.

- 1224 Crespo-Villanueva, A., Gumí-Audenis, B., Sanz, F., Artzner, F., Mériadec, C., Rousseau, F., Lopez,
1225 C., Giannotti, M. I., & Guyomarc'h, F. (2018). Casein interaction with lipid membranes:
1226 Are the phase state or charge density of the phospholipids affecting protein
1227 adsorption? *Biochimica Et Biophysica Acta. Biomembranes*, 1860(12), 2588–2598.
1228 <https://doi.org/10.1016/j.bbamem.2018.09.016>
- 1229 Dai, J., & Sheetz, M. P. (1999). Membrane Tether Formation from Blebbing Cells. *Biophysical*
1230 *Journal*, 77(6), 3363–3370.
- 1231 Daillant, J., Bellet-Amalric, E., Braslau, A., Charitat, T., Fragneto, G., Graner, F., Mora, S.,
1232 Rieutord, F., & Stidder, B. (2005). Structure and fluctuations of a single floating lipid
1233 bilayer. *Proceedings of the National Academy of Sciences of the United States of*
1234 *America*, 102(33), 11639.
- 1235 Davis, J. H., Clair, J. J., & Juhasz, J. (2009). Phase Equilibria in DOPC/DPPC-d62/Cholesterol
1236 Mixtures. *Biophysical Journal*, 96(2), 521–539.
1237 <https://doi.org/10.1016/j.bpj.2008.09.042>
- 1238 Deamer, D. W. (2010). From “banghasomes” to liposomes: A memoir of Alec Bangham, 1921-
1239 2010. *The FASEB Journal : Official Publication of the Federation of American Societies*
1240 *for Experimental Biology*, 24(5), 1308–1310. <https://doi.org/10.1096/fj.10-0503>
- 1241 Dieluweit, S., Csiszar, A., Rubner, W., Fleischhauer, J., Houben, S., & Merkel, R. (2010).
1242 Mechanical Properties of Bare and Protein-Coated Giant Unilamellar Phospholipid
1243 Vesicles. A Comparative Study of Micropipet Aspiration and Atomic Force Microscopy.
1244 *Langmuir*, 26(13), 11041–11049. <https://doi.org/10.1021/la1005242>
- 1245 Dimova, R. (2019). Giant Vesicles and Their Use in Assays for Assessing Membrane Phase State,
1246 Curvature, Mechanics, and Electrical Properties. *Annual Review of Biophysics*, 48(1),
1247 93–119. <https://doi.org/10.1146/annurev-biophys-052118-115342>
- 1248 Doktorova, M., Heberle, F. A., Eicher, B., Standaert, R. F., Katsaras, J., London, E., Pabst, G., &
1249 Marquardt, D. (2018). Preparation of asymmetric phospholipid vesicles for use as cell

- 1250 membrane models. *Nature Protocols*, *13*(9), 2086–2101.
- 1251 <https://doi.org/10.1038/s41596-018-0033-6>
- 1252 Domenech, O., Redondo, L., Picas, L., Morros, A., Montero, M. T., & Hernandez-Borrell, J.
- 1253 (2007). Atomic force microscopy characterization of supported planar bilayers that
- 1254 mimic the mitochondrial inner membrane. *Journal of Molecular Recognition*, *20*(6),
- 1255 546–553. <https://doi.org/10.1002/jmr.849>
- 1256 Dufrêne, Y. F., Ando, T., Garcia, R., Alsteens, D., Martinez-Martin, D., Engel, A., Gerber, C., &
- 1257 Müller, D. J. (2017). Imaging modes of atomic force microscopy for application in
- 1258 molecular and cell biology. *Nature Nanotechnology*, *12*, 295.
- 1259 <https://doi.org/10.1038/nnano.2017.45>
- 1260 Dufrene, Y. F., Barger, W. R., Green, J. B. D., & Lee, G. U. (1997). Nanometer-scale surface
- 1261 properties of mixed phospholipid monolayers and bilayers. *Langmuir*, *13*(18), 4779–
- 1262 4784. <https://doi.org/10.1021/la970221r>
- 1263 Dufrene, Y. F., Boland, T., Schneider, J. W., Barger, W. R., & Lee, G. U. (1998). Characterization
- 1264 of the physical properties of model biomembranes at the nanometer scale with the
- 1265 atomic force microscope. *Faraday Discussions*, *111*, 79–94.
- 1266 Dufrêne, Y. F., & Lee, G. U. (2000). Advances in the characterization of supported lipid films
- 1267 with the atomic force microscope. *Biochimica et Biophysica Acta (BBA) -*
- 1268 *Biomembranes*, *1509*(1), 14–41. [https://doi.org/10.1016/S0005-2736\(00\)00346-1](https://doi.org/10.1016/S0005-2736(00)00346-1)
- 1269 Ehrig, J., Petrov, E. P., & Schwille, P. (2011). Phase separation and near-critical fluctuations in
- 1270 two-component lipid membranes: Monte Carlo simulations on experimentally relevant
- 1271 scales. *New Journal of Physics*, *13*(4), 045019. [https://doi.org/10.1088/1367-](https://doi.org/10.1088/1367-2630/13/4/045019)
- 1272 [2630/13/4/045019](https://doi.org/10.1088/1367-2630/13/4/045019)
- 1273 El Kirat, K., Morandat, S., & Dufrene, Y. F. (2010). Nanoscale analysis of supported lipid bilayers
- 1274 using atomic force microscopy. *Biochimica Et Biophysica Acta-Biomembranes*, *1798*(4),
- 1275 750–765. <https://doi.org/10.1016/j.bbamem.2009.07.026>

- 1276 Evans, E, & Ritchie, K. (1997). Dynamic strength of molecular adhesion bonds. *Biophysical*
1277 *Journal*, 72(4), 1541–1555.
- 1278 Evans, E, & Yeung, A. (1994). Hidden dynamics in rapid changes of bilayer shape. *Chemistry and*
1279 *Physics of Lipids*, 73(1), 39–56. [https://doi.org/10.1016/0009-3084\(94\)90173-2](https://doi.org/10.1016/0009-3084(94)90173-2)
- 1280 Evans, Evan, Heinrich, V., Ludwig, F., & Rawicz, W. (2003). Dynamic Tension Spectroscopy and
1281 Strength of Biomembranes. *Biophysical Journal*, 85(4), 2342–2350.
- 1282 Fidorra, M., Heimburg, T., & Seeger, H. M. (2009). Melting of individual lipid components in
1283 binary lipid mixtures studied by FTIR spectroscopy, DSC and Monte Carlo simulations.
1284 *Biochimica Et Biophysica Acta-Biomembranes*, 1788(3), 600–607.
1285 <https://doi.org/10.1016/j.bbamem.2008.12.003>
- 1286 Florin, E. L., Moy, V. T., & Gaub, H. E. (1994). Adhesion forces between individual ligand-
1287 receptor pairs. *Science*, 264(5157), 415 LP – 417.
1288 <https://doi.org/10.1126/science.8153628>
- 1289 Franz, V., Loi, S., Muller, H., Bamberg, E., & Butt, H. H. (2002). Tip penetration through lipid
1290 bilayers in atomic force microscopy. *Colloids and Surfaces B-Biointerfaces*, 23(2–3),
1291 191–200.
- 1292 García-Arribas, A. B., Alonso, A., & Goñi, F. M. (2016). Cholesterol interactions with ceramide
1293 and sphingomyelin. *Chemistry and Physics of Lipids*, 199, 26–34.
1294 <https://doi.org/10.1016/j.chemphyslip.2016.04.002>
- 1295 García-Arribas, A. B., González-Ramírez, E. J., Sot, J., Areso, I., Alonso, A., & Goñi, F. M. (2017).
1296 Complex Effects of 24:1 Sphingolipids in Membranes Containing
1297 Dioleoylphosphatidylcholine and Cholesterol. *Langmuir*, 33(22), 5545–5554.
1298 <https://doi.org/10.1021/acs.langmuir.7b00162>
- 1299 Garcia-Manyes, S, Guell, A. G., Gorostiza, P., & Sanz, F. (2005). Nanomechanics of silicon
1300 surfaces with atomic force microscopy: An insight to the first stages of plastic
1301 deformation. *Journal of Chemical Physics*, 123(11). <https://doi.org/10.1063/1.2035094>

- 1302 Garcia-Manyes, S, Oncins, G., & Sanz, F. (2005a). Effect of ion-binding and chemical
1303 phospholipid structure on the nanomechanics of lipid bilayers studied by force
1304 spectroscopy. *Biophysical Journal*, *89*, 1812–1826.
1305 <https://doi.org/10.1529/biophysj.105.064030>
- 1306 Garcia-Manyes, S, Oncins, G., & Sanz, F. (2005b). Effect of temperature on the nanomechanics
1307 of lipid bilayers studied by force spectroscopy. *Biophysical Journal*, *89*(6), 4261–4274.
1308 <https://doi.org/10.1529/biophysj.105.065581>
- 1309 Garcia-Manyes, S, Redondo-Morata, L., Oncins, G., & Sanz, F. (2010). Nanomechanics of Lipid
1310 Bilayers: Heads or Tails? *Journal of the American Chemical Society*, *132*(37), 12874–
1311 12886. <https://doi.org/10.1021/ja1002185>
- 1312 Garcia-Manyes, S, & Sanz, F. (2010). Nanomechanics of lipid bilayers by force spectroscopy
1313 with AFM: A perspective. *Biochimica Et Biophysica Acta-Biomembranes*, *1798*(4), 741–
1314 749. <https://doi.org/10.1016/j.bbamem.2009.12.019>
- 1315 Garcia-Manyes, Sergi, Redondo-Morata, L., Oncins, G., & Sanz, F. (2010). Nanomechanics of
1316 Lipid Bilayers: Heads or Tails? *Journal of the American Chemical Society*, *132*(37),
1317 12874–12886. <https://doi.org/10.1021/ja1002185>
- 1318 Giannotti, M. I., & Vancso, G. J. (2007). Interrogation of single synthetic polymer chains and
1319 polysaccharides by AFM-based force spectroscopy. *ChemPhysChem*, *8*(16).
1320 <https://doi.org/10.1002/cphc.200700175>
- 1321 Giles, R., Cleveland, J. P., Manne, S., Hansma, P. K., Drake, B., Maivald, P., Boles, C., Gurley, J.,
1322 & Elings, V. (1993). Noncontact force microscopy in liquids. *Applied Physics Letters*,
1323 *63*(5), 617–618. <https://doi.org/10.1063/1.109967>
- 1324 Gillissen, J. J. J., Jackman, J. A., Tabaei, S. R., Yoon, B. K., & Cho, N.-J. (2017). Quartz Crystal
1325 Microbalance Model for Quantitatively Probing the Deformation of Adsorbed Particles
1326 at Low Surface Coverage. *Analytical Chemistry*, *89*(21), 11711–11718.
1327 <https://doi.org/10.1021/acs.analchem.7b03179>

- 1328 Goñi, F. M. (2019a). "Rafts": A nickname for putative transient nanodomains. *Chemistry and*
1329 *Physics of Lipids*, 218, 34–39. <https://doi.org/10.1016/j.chemphyslip.2018.11.006>
- 1330 Goñi, F. M. (2019b). "Rafts": A nickname for putative transient nanodomains. In *Chemistry and*
1331 *Physics of Lipids* (Vol. 218, pp. 34–39). Elsevier Ireland Ltd.
1332 <https://doi.org/10.1016/j.chemphyslip.2018.11.006>
- 1333 González-Ramírez, E. J., Artetxe, I., García-Arribas, A. B., Goñi, F. M., & Alonso, A. (2019).
1334 Homogeneous and Heterogeneous Bilayers of Ternary Lipid Compositions Containing
1335 Equimolar Ceramide and Cholesterol. *Langmuir*, 35(15), 5305–5315.
1336 <https://doi.org/10.1021/acs.langmuir.9b00324>
- 1337 Gumí-Audenis, B., Costa, L., Carlá, F., Comin, F., Sanz, F., & Giannotti, M. I. (2016a). Structure
1338 and nanomechanics of model membranes by atomic force microscopy and
1339 spectroscopy: Insights into the role of cholesterol and sphingolipids. *Membranes*, 6(4).
1340 <https://doi.org/10.3390/membranes6040058>
- 1341 Gumí-Audenis, B., Costa, L., Carlá, F., Comin, F., Sanz, F., & Giannotti, M. I. (2016b). Structure
1342 and nanomechanics of model membranes by atomic force microscopy and
1343 spectroscopy: Insights into the role of cholesterol and sphingolipids. *Membranes*, 6(4).
1344 <https://doi.org/10.3390/membranes6040058>
- 1345 Gumí-Audenis, B., Costa, L., Redondo-Morata, L., Milhiet, P.-E., Sanz, F., Felici, R., Giannotti, M.
1346 I., & Carlà, F. (2018). In-plane molecular organization of hydrated single lipid bilayers:
1347 DPPC: cholesterol. *Nanoscale*, 10(1). <https://doi.org/10.1039/c7nr07510c>
- 1348 Gumí-Audenis, B., Costa, L., Redondo-Morata, L., Milhiet, P.-E., Sanz, F., Felici, R., Giannotti, M.
1349 I., & Carla, F. (2018). In-plane molecular organization of hydrated single lipid bilayers:
1350 DPPC:cholesterol. *Nanoscale*, 10(1), 87–92. <https://doi.org/10.1039/c7nr07510c>
- 1351 Gumí-Audenis, Berta, Costa, L., Ferrer-Tasies, L., Ratera, I., Ventosa, N., Sanz, F., & Giannotti,
1352 M. I. (2018). Pulling lipid tubes from supported bilayers unveils the underlying

- 1353 substrate contribution to the membrane mechanics. *Nanoscale*.
- 1354 <https://doi.org/10.1039/C8NR03249A>
- 1355 Gumí-Audenis, Berta, Sanz, F., & Giannotti, M. I. (2015). Impact of galactosylceramides on the
1356 nanomechanical properties of lipid bilayer models: An AFM-force spectroscopy study.
1357 *Soft Matter*, *11*(27), 5447–5454. <https://doi.org/10.1039/C5SM01252J>
- 1358 Guyomarc’h, F., Zou, S., Chen, M., Milhiet, P.-E., Godefroy, C., Vié, V., & Lopez, C. (2014). Milk
1359 Sphingomyelin Domains in Biomimetic Membranes and the Role of Cholesterol:
1360 Morphology and Nanomechanical Properties Investigated Using AFM and Force
1361 Spectroscopy. *Langmuir*, *30*(22), 6516–6524. <https://doi.org/10.1021/la501640y>
- 1362 Hardy, G. J., Nayak, R., & Zauscher, S. (2013). Model cell membranes: Techniques to form
1363 complex biomimetic supported lipid bilayers via vesicle fusion. *Current Opinion in*
1364 *Colloid & Interface Science*, *18*(5), 448–458.
1365 <https://doi.org/10.1016/j.cocis.2013.06.004>
- 1366 Hasan, I. Y., & Mechler, A. (2015). Viscoelastic changes measured in partially suspended single
1367 bilayer membranes. *Soft Matter*, *11*(27), 5571–5579.
1368 <https://doi.org/10.1039/C5SM00278H>
- 1369 Hassinger, J. E., Oster, G., Drubin, D. G., & Rangamani, P. (2017). Design principles for robust
1370 vesiculation in clathrin-mediated endocytosis. *Proceedings of the National Academy of*
1371 *Sciences*, *114*(7), E1118 LP-E1127. <https://doi.org/10.1073/pnas.1617705114>
- 1372 Heimburg, T. (1998). Mechanical aspects of membrane thermodynamics. Estimation of the
1373 mechanical properties of lipid membranes close to the chain melting transition from
1374 calorimetry. *Biochimica Et Biophysica Acta-Biomembranes*, *1415*(1), 147–162.
1375 [https://doi.org/10.1016/s0005-2736\(98\)00189-8](https://doi.org/10.1016/s0005-2736(98)00189-8)
- 1376 Hill, T. L. (2013). *Thermodynamics of Small Systems/* (Reprint). Dover Publications Inc.

- 1377 Hochmuth, F. M., Shao, J. Y., Dai, J., & Sheetz, M. P. (1996). Deformation and flow of
1378 membrane into tethers extracted from neuronal growth cones. *Biophysical Journal*,
1379 *70*(1), 358–369.
- 1380 Hohner, A. O., David, M. P. C., & Rädler, J. O. (2010). Controlled solvent-exchange deposition of
1381 phospholipid membranes onto solid surfaces. *Biointerphases*, *5*(1), 1–8.
1382 <https://doi.org/10.1116/1.3319326>
- 1383 Hugel, T., & Seitz, M. (2001). The Study of Molecular Interactions by AFM Force Spectroscopy.
1384 *Macromolecular Rapid Communications*, *22*(13), 989–1016.
1385 [https://doi.org/10.1002/1521-3927\(20010901\)22:13<989::AID-MARC989>3.0.CO;2-D](https://doi.org/10.1002/1521-3927(20010901)22:13<989::AID-MARC989>3.0.CO;2-D)
- 1386 Hung, W.-C., Lee, M.-T., Chen, F.-Y., & Huang, H. W. (2007). The condensing effect of
1387 cholesterol in lipid bilayers. *Biophysical Journal*, *92*(11), 3960–3967.
1388 <https://doi.org/10.1529/biophysj.106.099234>
- 1389 Hurley, J. H., Boura, E., Carlson, L.-A., & Rózycki, B. (2010). Membrane Budding. *Cell*, *143*(6),
1390 875–887. <https://doi.org/10.1016/j.cell.2010.11.030>
- 1391 Ira, Zou, S., Ramirez, D. M. C., Vanderlip, S., Ogilvie, W., Jakubek, Z. J., & Johnston, L. J. (2009).
1392 Enzymatic generation of ceramide induces membrane restructuring: Correlated AFM
1393 and fluorescence imaging of supported bilayers. *Journal of Structural Biology*, *168*(1),
1394 78–89. <https://doi.org/10.1016/j.jsb.2009.03.014>
- 1395 Jiménez-Rojo, N., García-Arribas, A. B., Sot, J., Alonso, A., & Goñi, F. M. (2014). Lipid bilayers
1396 containing sphingomyelins and ceramides of varying N-acyl lengths: A glimpse into
1397 sphingolipid complexity. *Biochimica et Biophysica Acta - Biomembranes*, *1838*(1
1398 PARTB), 456–464. <https://doi.org/10.1016/j.bbamem.2013.10.010>
- 1399 Jing, Y., Trefna, H., Persson, M., Kasemo, B., & Svedhem, S. (2013). Formation of supported
1400 lipid bilayers on silica: Relation to lipid phase transition temperature and liposome
1401 size. *Soft Matter*, *10*(1), 187–195. <https://doi.org/10.1039/C3SM50947H>

- 1402 Johnston, L. J. (2007). Nanoscale imaging of domains in supported lipid membranes. *Langmuir*:
1403 *The ACS Journal of Surfaces and Colloids*, 23(11), 5886–5895.
1404 <https://doi.org/10.1021/la070108t>
- 1405 Kahya, N., Scherfeld, D., Bacia, K., & Schwille, P. (2004). Lipid domain formation and dynamics
1406 in giant unilamellar vesicles explored by fluorescence correlation spectroscopy. *Journal*
1407 *of Structural Biology*, 147(1), 77–89. <https://doi.org/10.1016/j.jsb.2003.09.021>
- 1408 Kechagia, J. Z., Ivaska, J., & Roca-Cusachs, P. (2019). Integrins as biomechanical sensors of the
1409 microenvironment. *Nature Reviews Molecular Cell Biology*, 20(8), 457–473.
1410 <https://doi.org/10.1038/s41580-019-0134-2>
- 1411 Keller, C. A., & Kasemo, B. (1998). Surface specific kinetics of lipid vesicle adsorption measured
1412 with a quartz crystal microbalance. *Biophysical Journal*, 75(3), 1397–1402.
- 1413 Keller, D., Larsen, N. B., Moller, I. M., & Mouritsen, O. G. (2005). Decoupled phase transitions
1414 and grain-boundary melting in supported phospholipid bilayers. *Physical Review*
1415 *Letters*, 94(2). <https://doi.org/10.1103/PhysRevLett.94.025701>
- 1416 Kodera, N., Yamamoto, D., Ishikawa, R., & Ando, T. (2010). Video imaging of walking myosin V
1417 by high-speed atomic force microscopy. *Nature*, 468(7320).
1418 <https://doi.org/10.1038/nature09450>
- 1419 Kurniawan, J., Ventrici de Souza, J. F., Dang, A. T., Liu, G., & Kuhl, T. L. (2018). Preparation and
1420 Characterization of Solid-Supported Lipid Bilayers Formed by Langmuir–Blodgett
1421 Deposition: A Tutorial. *Langmuir*, 34(51), 15622–15639.
1422 <https://doi.org/10.1021/acs.langmuir.8b03504>
- 1423 Lee, G. U., Chrisey, L. A., & Colton, R. J. (1994). DIRECT MEASUREMENT OF THE FORCES
1424 BETWEEN COMPLEMENTARY STRANDS OF DNA. *Science*, 266(5186), 771–773.
1425 <https://doi.org/10.1126/science.7973628>
- 1426 Leonenko, Z. V, Finot, E., Ma, H., Dahms, T. E. S., & Cramb, D. T. (2004). Investigation of
1427 temperature-induced phase transitions in DOPC and DPPC phospholipid bilayers using

- 1428 temperature-controlled scanning force microscopy. *Biophysical Journal*, 86(6), 3783–
1429 3793. <https://doi.org/10.1529/biophysj.103.036681>
- 1430 Leonenko, Z. V., Finot, E., Ma, H., Dahms, T. E. S., & Cramb, D. T. (2004). Investigation of
1431 temperature-induced phase transitions in DOPC and DPPC phospholipid bilayers using
1432 temperature-controlled scanning force microscopy. *Biophysical Journal*, 86(6), 3783–
1433 3793. <https://doi.org/10.1529/biophysj.103.036681>
- 1434 Lin, D. C., Dimitriadis, E. K., & Horkay, F. (2007). Robust strategies for automated AFM force
1435 curve analysis—I. Non-adhesive indentation of soft, inhomogeneous materials. *Journal*
1436 *of Biomechanical Engineering*, 129(3), 430–440. <https://doi.org/10.1115/1.2720924>
- 1437 Lin, W.-C., Blanchette, C. D., & Longo, M. L. (2007). Fluid-Phase Chain Unsaturation Controlling
1438 Domain Microstructure and Phase in Ternary Lipid Bilayers Containing GalCer and
1439 Cholesterol. *Biophysical Journal*, 92(8), 2831–2841.
1440 <https://doi.org/10.1529/biophysj.106.095422>
- 1441 Lind, T. K., & Cárdenas, M. (2016). Understanding the formation of supported lipid bilayers via
1442 vesicle fusion-A case that exemplifies the need for the complementary method
1443 approach (Review). *Biointerphases*, 11(2), 020801. <https://doi.org/10.1116/1.4944830>
- 1444 Lipowsky, R., & Seifert, U. (1991). Adhesion of Vesicles and Membranes. *Molecular Crystals*
1445 *and Liquid Crystals*, 202(1), 17–25. <https://doi.org/10.1080/00268949108035656>
- 1446 Loi, S, Sun, G., Franz, V., & Butt, H. J. (2002). Rupture of molecular thin films observed in
1447 atomic force microscopy. II. Experiment. *Physical Review E*, 66(3).
1448 <https://doi.org/10.1103/PhysRevE.66.031602>
- 1449 Loi, Simona, Sun, G., Franz, V., & Butt, H.-J. (2002). Rupture of molecular thin films observed in
1450 atomic force microscopy. II. Experiment. *Phys Rev E Stat Nonlin Soft Matter Phys*, 66(3
1451 Pt 1), 31602.
- 1452 Losada-Pérez, P., Jiménez-Monroy, K. L., Grinsven, B. van, Leys, J., Janssens, S. D., Peeters, M.,
1453 Glorieux, C., Thoen, J., Haenen, K., Ceuninck, W. D., & Wagner, P. (2014). Phase

- 1454 transitions in lipid vesicles detected by a complementary set of methods: Heat-transfer
1455 measurements, adiabatic scanning calorimetry, and dissipation-mode quartz crystal
1456 microbalance. *Physica Status Solidi (a)*, 211(6), 1377–1388.
1457 <https://doi.org/10.1002/pssa.201431060>
- 1458 Losada-Pérez, P., Khorshid, M., Yongabi, D., & Wagner, P. (2015). Effect of Cholesterol on the
1459 Phase Behavior of Solid-Supported Lipid Vesicle Layers. *The Journal of Physical
1460 Chemistry B*, 119(15), 4985–4992. <https://doi.org/10.1021/acs.jpcc.5b00712>
- 1461 Losada-Pérez, P., Mertens, N., de Medio-Vasconcelos, B., Slenders, E., Leys, J., Peeters, M., van
1462 Grinsven, B., Gruber, J., Glorieux, C., Pfeiffer, H., Wagner, P., & Thoen, J. (2015). *Phase
1463 Transitions of Binary Lipid Mixtures: A Combined Study by Adiabatic Scanning
1464 Calorimetry and Quartz Crystal Microbalance with Dissipation Monitoring* [Research
1465 Article]. *Advances in Condensed Matter Physics*; Hindawi.
1466 <https://doi.org/10.1155/2015/479318>
- 1467 Mabrey, S., & Sturtevant, J. M. (1976). Investigation of phase transitions of lipids and lipid
1468 mixtures by high sensitivity differential scanning calorimetry. *Proceedings of the
1469 National Academy of Sciences of the United States of America*, 73(11), 3862–3866.
1470 <https://doi.org/10.1073/pnas.73.11.3862>
- 1471 Maeda, N., Senden, T. J., & di Meglio, J.-M. (2002). Micromanipulation of phospholipid bilayers
1472 by atomic force microscopy. *Biochimica et Biophysica Acta (BBA) - Biomembranes*,
1473 1564(1), 165–172.
- 1474 Mannock, D. A., Lewis, R. N. A. H., & McElhaney, R. N. (2010). A calorimetric and spectroscopic
1475 comparison of the effects of ergosterol and cholesterol on the thermotropic phase
1476 behavior and organization of dipalmitoylphosphatidylcholine bilayer membranes.
1477 *Biochimica Et Biophysica Acta*, 1798(3), 376–388.
1478 <https://doi.org/10.1016/j.bbamem.2009.09.002>

- 1479 Marcus, W. D., & Hochmuth, R. M. (2002). Experimental Studies of Membrane Tethers Formed
1480 from Human Neutrophils. *Annals of Biomedical Engineering*, 30(10), 1273–1280.
1481 <https://doi.org/10.1114/1.1528614>
- 1482 Marszalek, P E, Lu, H., Li, H. B., Carrion-Vazquez, M., Oberhauser, A. F., Schulten, K., &
1483 Fernandez, J. M. (1999). Mechanical unfolding intermediates in titin modules. *Nature*,
1484 402(6757), 100–103.
- 1485 Marszalek, Piotr E, Li, H., & Fernandez, J. M. (2001). Fingerprinting polysaccharides with single-
1486 molecule atomic force microscopy. *Nat Biotech*, 19(3), 258–262.
- 1487 Mennicke, U., & Salditt, T. (2002). Preparation of solid-supported lipid bilayers by spin-coating.
1488 *Langmuir*, 18(21), 8172–8177. <https://doi.org/10.1021/la025863f>
- 1489 Mierzwa, B. E., Chiaruttini, N., Redondo-Morata, L., von Filseck, J. M., Koenig, J., Larios, J.,
1490 Poser, I., Mueller-Reichert, T., Scheuring, S., Roux, A., & Gerlich, D. W. (2017). Dynamic
1491 subunit turnover in ESCRT-III assemblies is regulated by Vps4 to mediate membrane
1492 remodelling during cytokinesis. *Nature Cell Biology*, 19(7), 787–+.
1493 <https://doi.org/10.1038/ncb3559>
- 1494 Mills, T. T., Huang, J., Feigenson, G. W., & Nagle, J. F. (2009). Effects of cholesterol and
1495 unsaturated DOPC lipid on chain packing of saturated gel-phase DPPC bilayers. *General*
1496 *Physiology and Biophysics*, 28(2), 126–139.
- 1497 Mingeot-Leclercq, M. P., Deleu, M., Brasseur, R., & Dufrene, Y. F. (2008). Atomic force
1498 microscopy of supported lipid bilayers. *Nature Protocols*, 3(10), 1654–1659.
1499 <https://doi.org/10.1038/nprot.2008.149>
- 1500 Miyoshi, T., Lönnfors, M., Peter Slotte, J., & Kato, S. (2014). A detailed analysis of partial
1501 molecular volumes in DPPC/cholesterol binary bilayers. *Biochimica Et Biophysica Acta*,
1502 1838(12), 3069–3077. <https://doi.org/10.1016/j.bbamem.2014.07.004>

- 1503 Morandat, S., Azouzi, S., Beauvais, E., Mastouri, A., & El Kirat, K. (2013). Atomic force
1504 microscopy of model lipid membranes. *Analytical and Bioanalytical Chemistry*, 405(5),
1505 1445–1461. <https://doi.org/10.1007/s00216-012-6383-y>
- 1506 Mouritsen, O. G., & Bloom, M. (1984). MATTRESS MODEL OF LIPID-PROTEIN INTERACTIONS IN
1507 MEMBRANES. *Biophysical Journal*, 46(2), 141–153.
- 1508 Nagle, J. F., & Tristram-Nagle, S. (2000). Structure of lipid bilayers. *Biochimica Et Biophysica*
1509 *Acta-Reviews on Biomembranes*, 1469(3), 159–195. [https://doi.org/10.1016/s0304-](https://doi.org/10.1016/s0304-4157(00)00016-2)
1510 [4157\(00\)00016-2](https://doi.org/10.1016/s0304-4157(00)00016-2)
- 1511 Nawaz, S., Sánchez, P., Schmitt, S., Snaidero, N., Mitkovski, M., Velte, C., Brückner, B. R.,
1512 Alexopoulos, I., Czopka, T., Jung, S. Y., Rhee, J. S., Janshoff, A., Witke, W., Schaap, I. A.
1513 T., Lyons, D. A., & Simons, M. (2015). Actin Filament Turnover Drives Leading Edge
1514 Growth during Myelin Sheath Formation in the Central Nervous System.
1515 *Developmental Cell*, 34(2), 139–151. <https://doi.org/10.1016/j.devcel.2015.05.013>
- 1516 Neupane, S., De Smet, Y., Renner, F. U., & Losada-Pérez, P. (2018). Quartz Crystal Microbalance
1517 With Dissipation Monitoring: A Versatile Tool to Monitor Phase Transitions in
1518 Biomimetic Membranes. *Frontiers in Materials*, 5.
1519 <https://doi.org/10.3389/fmats.2018.00046>
- 1520 Noy, A., Vezenov, D. V., & Lieber, C. M. (1997). CHEMICAL FORCE MICROSCOPY. *Annual Review*
1521 *of Materials Science*, 27(1), 381–421.
1522 <https://doi.org/10.1146/annurev.matsci.27.1.381>
- 1523 Olsson, A. L. J., Quevedo, I. R., He, D., Basnet, M., & Tufenkji, N. (2013). Using the Quartz
1524 Crystal Microbalance with Dissipation Monitoring to Evaluate the Size of Nanoparticles
1525 Deposited on Surfaces. *ACS Nano*, 7(9), 7833–7843.
1526 <https://doi.org/10.1021/nn402758w>

- 1527 Pan, J., Mills, T. T., Tristram-Nagle, S., & Nagle, J. F. (2008). Cholesterol perturbs lipid bilayers
1528 nonuniversally. *Physical Review Letters*, *100*(19), 198103.
1529 <https://doi.org/10.1103/PhysRevLett.100.198103>
- 1530 Parot, P., Dufrêne, Y. F., Hinterdorfer, P., Le Grimellec, C., Navajas, D., Pellequer, J. L., &
1531 Scheuring, S. (2007). Past, present and future of atomic force microscopy in life
1532 sciences and medicine. *J Mol Recognit*, *20*(6), 418–431.
1533 <https://doi.org/10.1002/jmr.857>
- 1534 Peschel, A., Langhoff, A., Uhl, E., Dathathreyan, A., Haindl, S., Johannsmann, D., & Reviakine, I.
1535 (2016). Lipid phase behavior studied with a quartz crystal microbalance: A technique
1536 for biophysical studies with applications in screening. *The Journal of Chemical Physics*,
1537 *145*(20), 204904. <https://doi.org/10.1063/1.4968215>
- 1538 Picas, L., Montero, M. T., Morros, A., Cabanas, M. E., Seantier, B., Milhiet, P.-E., & Hernandez-
1539 Borrell, J. (2009). Calcium-Induced Formation of Subdomains in
1540 Phosphatidylethanolamine-Phosphatidylglycerol Bilayers: A Combined DSC, (31)P
1541 NMR, and AFM Study. *Journal of Physical Chemistry B*, *113*(14), 4648–4655.
1542 <https://doi.org/10.1021/jp8102468>
- 1543 Picas, L., Rico, F., & Scheuring, S. (2012). Direct Measurement of the Mechanical Properties of
1544 Lipid Phases in Supported Bilayers. *Biophysical Journal*, *102*(1), L1–L3.
1545 <https://doi.org/10.1016/j.bpj.2011.11.4001>
- 1546 Piggot, T. J., Allison, J. R., Sessions, R. B., & Essex, J. W. (2017). On the Calculation of Acyl Chain
1547 Order Parameters from Lipid Simulations. *Journal of Chemical Theory and
1548 Computation*, *13*(11), 5683–5696. <https://doi.org/10.1021/acs.jctc.7b00643>
- 1549 Pinkwart, K., Schneider, F., Lukoseviciute, M., Sauka-Spengler, T., Lyman, E., Eggeling, C., &
1550 Sezgin, E. (2019). Nanoscale dynamics of cholesterol in the cell membrane. *Journal of
1551 Biological Chemistry*, *294*(34), 12599–12609.
1552 <https://doi.org/10.1074/jbc.RA119.009683>

- 1553 Pramanik, S. K., Seneca, S., Ethirajan, A., Neupane, S., Renner, F. U., & Losada-Pérez, P. (2016).
1554 Ionic strength dependent vesicle adsorption and phase behavior of anionic
1555 phospholipids on a gold substrate. *Biointerphases*, *11*(1), 019006.
1556 <https://doi.org/10.1116/1.4939596>
- 1557 Radmacher, M. (1997). Measuring the elastic properties of biological samples with the AFM.
1558 *IEEE Engineering in Medicine and Biology Magazine*, *16*(2), 47–57.
1559 <https://doi.org/10.1109/51.582176>
- 1560 Rascol, E., Devoisselle, J.-M., & Chopineau, J. (2016). The relevance of membrane models to
1561 understand nanoparticles–cell membrane interactions. *Nanoscale*, *8*(9), 4780–4798.
1562 <https://doi.org/10.1039/C5NR07954C>
- 1563 Rawicz, W., Olbrich, K. C., McIntosh, T., Needham, D., & Evans, E. (2000). Effect of chain length
1564 and unsaturation on elasticity of lipid bilayers. *Biophysical Journal*, *79*(1), 328–339.
- 1565 Redondo-Morata, L, Giannotti, M. I., & Sanz, F. (2012a). AFM-Based Force-Clamp Monitors
1566 Lipid Bilayer Failure Kinetics. *Langmuir*, *28*(15), 6403–6410.
1567 <https://doi.org/10.1021/la3005147>
- 1568 Redondo-Morata, L, Giannotti, M. I., & Sanz, F. (2012b). Influence of Cholesterol on the Phase
1569 Transition of Lipid Bilayers: A Temperature-Controlled Force Spectroscopy Study.
1570 *Langmuir*, *28*(35), 12851–12860. <https://doi.org/10.1021/la302620t>
- 1571 Redondo-Morata, L, Giannotti, M. I., & Sanz, F. (2012c). Influence of Cholesterol on the Phase
1572 Transition of Lipid Bilayers: A Temperature-Controlled Force Spectroscopy Study.
1573 *Langmuir*, *28*(35), 12851–12860. <https://doi.org/10.1021/la302620t>
- 1574 Redondo-Morata, L., Giannotti, M. I., & Sanz, F. (2012). Stability of Lipid Bilayers as Model
1575 Membranes: Atomic Force Microscopy and Spectroscopy Approach. In *Atomic Force*
1576 *Microscopy in Liquid: Biological Applications*.
1577 <https://doi.org/10.1002/9783527649808.ch10>

- 1578 Redondo-Morata, L, Giannotti, M. I., & Sanz, F. (2014). Structural impact of cations on lipid
1579 bilayer models: Nanomechanical properties by AFM-force spectroscopy. *Molecular*
1580 *Membrane Biology*, 31(1), 17–28. <https://doi.org/10.3109/09687688.2013.868940>
- 1581 Redondo-Morata, L, Sanford, R. L., Andersen, O. S., & Scheuring, S. (2016). Effect of Statins on
1582 the Nanomechanical Properties of Supported Lipid Bilayers. *Biophysical Journal*,
1583 111(2), 363–372. <https://doi.org/10.1016/j.bpj.2016.06.016>
- 1584 Redondo-Morata, Lorena, Oncins, G., & Sanz, F. (2012). Force Spectroscopy Reveals the Effect
1585 of Different Ions in the Nanomechanical Behavior of Phospholipid Model Membranes:
1586 The Case of Potassium Cation. *Biophysical Journal*, 102(1), 66–74.
1587 <https://doi.org/10.1016/j.bpj.2011.10.051>
- 1588 Reimhult, E., Hook, F., & Kasemo, B. (2003). Intact vesicle adsorption and supported
1589 biomembrane formation from vesicles in solution: Influence of surface chemistry,
1590 vesicle size, temperature, and osmotic pressure. *Langmuir*, 19(5), 1681–1691.
1591 <https://doi.org/10.1021/la0263920>
- 1592 Relat-Goberna, J., Beedle Amy, E. M., & Garcia-Manyes, S. (2017). The Nanomechanics of Lipid
1593 Multibilayer Stacks Exhibits Complex Dynamics. *Small*, 13(24), 1700147.
1594 <https://doi.org/10.1002/smll.201700147>
- 1595 Reviakine, I., Gallego, M., Johannsmann, D., & Tellechea, E. (2012). Adsorbed liposome
1596 deformation studied with quartz crystal microbalance. *The Journal of Chemical Physics*,
1597 136(8), 084702. <https://doi.org/10.1063/1.3687351>
- 1598 Reviakine, I., Johannsmann, D., & Richter, R. P. (2011). Hearing What You Cannot See and
1599 Visualizing What You Hear: Interpreting Quartz Crystal Microbalance Data from
1600 Solvated Interfaces. *Analytical Chemistry*, 83(23), 8838–8848.
1601 <https://doi.org/10.1021/ac201778h>

- 1602 Richter, R., Mukhopadhyay, A., & Brisson, A. (2003). Pathways of Lipid Vesicle Deposition on
1603 Solid Surfaces: A Combined QCM-D and AFM Study. *Biophysical Journal*, 85(5), 3035–
1604 3047.
- 1605 Richter, R P. (2006). Formation of solid-supported lipid bilayers: An integrated view. *Langmuir*,
1606 22(8), 3497–3505. <https://doi.org/10.1021/la052687c>
- 1607 Richter, Ralf P, & Brisson, A. (2003). Characterization of Lipid Bilayers and Protein Assemblies
1608 Supported on Rough Surfaces by Atomic Force Microscopy. *Langmuir*, 19(5), 1632–
1609 1640. <https://doi.org/10.1021/la026427w>
- 1610 Richter, Ralf P, & Brisson, A. R. (2005). Following the Formation of Supported Lipid Bilayers on
1611 Mica: A Study Combining AFM, QCM-D, and Ellipsometry. *Biophysical Journal*, 88(5),
1612 3422–3433. <https://doi.org/10.1529/biophysj.104.053728>
- 1613 Rief, M., Oesterhelt, F., Heymann, B., & Gaub, H. E. (1997). Single Molecule Force Spectroscopy
1614 on Polysaccharides by Atomic Force Microscopy. *Science*, 275(5304), 1295 LP – 1297.
1615 <https://doi.org/10.1126/science.275.5304.1295>
- 1616 Rog, T., Pasenkiewicz-Gierula, M., Vattulainen, I., & Karttunen, M. (2009). Ordering effects of
1617 cholesterol and its analogues. *Biochimica Et Biophysica Acta-Biomembranes*, 1788(1),
1618 97–121. <https://doi.org/10.1016/j.bbamem.2008.08.022>
- 1619 Roux, A. (2013). The physics of membrane tubes: Soft templates for studying cellular
1620 membranes. *Soft Matter*, 9(29), 6726–6736.
- 1621 Sauerbrey, G. (1959). Verwendung von Schwingquarzen zur Wägung dünner Schichten und zur
1622 Mikrowägung. *Zeitschrift für Physik*, 155(2), 206–222.
1623 <https://doi.org/10.1007/BF01337937>
- 1624 Schmidtke, D. W., & Diamond, S. L. (2000). Direct Observation of Membrane Tethers Formed
1625 during Neutrophil Attachment to Platelets or P-Selectin under Physiological Flow. *The*
1626 *Journal of Cell Biology*, 149(3), 719.

- 1627 Schneider, J., Dufrene, Y. F., Barger, W. R., & Lee, G. U. (2000). Atomic force microscope image
1628 contrast mechanisms on supported lipid bilayers. *Biophysical Journal*, 79(2), 1107–
1629 1118.
- 1630 Sebaaly, C., Greige-Gerges, H., & Charcosset, C. (2019). Chapter 11—Lipid Membrane Models
1631 for Biomembrane Properties' Investigation (A. Basile & C. B. T.-C. T. and F. D. on (Bio-
1632 M. Charcosset, Eds.; pp. 311–340). Elsevier. [https://doi.org/10.1016/B978-0-12-](https://doi.org/10.1016/B978-0-12-813606-5.00011-7)
1633 [813606-5.00011-7](https://doi.org/10.1016/B978-0-12-813606-5.00011-7)
- 1634 Seeger, H. M., Di Cerbo, A., Alessandrini, A., & Facci, P. (2010). Supported Lipid Bilayers on
1635 Mica and Silicon Oxide: Comparison of the Main Phase Transition Behavior. *Journal of*
1636 *Physical Chemistry B*, 114(27), 8926–8933. <https://doi.org/10.1021/jp1026477>
- 1637 Sessa, G., & Weissmann, G. (1968). Phospholipid spherules (liposomes) as a model for
1638 biological membranes. *Journal of Lipid Research*, 9(3), 310–318.
- 1639 Shao, J.-Y., Ting-Beall, H. P., & Hochmuth, R. M. (1998). Static and dynamic lengths of
1640 neutrophil microvilli. *Proceedings of the National Academy of Sciences*, 95(12), 6797.
- 1641 Sheetz, M. P. (2001). Cell control by membrane-cytoskeleton adhesion. *Nature Reviews*
1642 *Molecular Cell Biology*, 2, 392.
- 1643 Shinoda, K., Shinoda, W., & Mikami, M. (2007). Molecular dynamics simulation of an archaeal
1644 lipid bilayer with sodium chloride. *Physical Chemistry Chemical Physics*, 9(5), 643–650.
1645 <https://doi.org/10.1039/b611543h>
- 1646 Simons, K., & Ikonen, E. (1997). Functional rafts in cell membranes. *Nature*, 387(6633), 569–
1647 572. <https://doi.org/10.1038/42408>
- 1648 Singer, S. J., & Nicolson, G. L. (1972). FLUID MOSAIC MODEL OF STRUCTURE OF CELL-
1649 MEMBRANES. *Science*, 175(4023), 720-. <https://doi.org/10.1126/science.175.4023.720>
- 1650 Siontorou, C. G., Nikoleli, G.-P., Nikolelis, D. P., & Karapetis, S. K. (2017). Artificial Lipid
1651 Membranes: Past, Present, and Future. *Membranes*, 7(3), 38.
1652 <https://doi.org/10.3390/membranes7030038>

- 1653 Steinkühler, J., Sezgin, E., Urbančič, I., Eggeling, C., & Dimova, R. (2019). Mechanical properties
1654 of plasma membrane vesicles correlate with lipid order, viscosity and cell density.
1655 *Communications Biology*, 2(1), 1–8. <https://doi.org/10.1038/s42003-019-0583-3>
- 1656 Strulson, M. K., & Maurer, J. A. (2011). Microcontact printing for creation of patterned lipid
1657 bilayers on tetraethylene glycol self-assembled monolayers. *Langmuir : The ACS*
1658 *Journal of Surfaces and Colloids*, 27(19), 12052–12057.
1659 <https://doi.org/10.1021/la201839w>
- 1660 Sullan, R M A, Li, J. K., Hao, C. C., Walker, G. C., & Zou, S. (2010). Cholesterol-Dependent
1661 Nanomechanical Stability of Phase-Segregated Multicomponent Lipid Bilayers.
1662 *Biophysical Journal*, 99(2), 507–516. <https://doi.org/10.1016/j.bpj.2010.04.044>
- 1663 Sullan, Ruby May A, Li, J. K., & Zou, S. (2009a). Direct Correlation of Structures and
1664 Nanomechanical Properties of Multicomponent Lipid Bilayers. *Langmuir*, 25(13), 7471–
1665 7477. <https://doi.org/10.1021/la900395w>
- 1666 Sullan, Ruby May A, Li, J. K., & Zou, S. (2009b). Quantification of the Nanomechanical Stability
1667 of Ceramide-Enriched Domains. *Langmuir*, 25(22), 12874–12877.
1668 <https://doi.org/10.1021/la903442s>
- 1669 Sun, M., Graham, J. S., Hegedüs, B., Marga, F., Zhang, Y., Forgacs, G., & Grandbois, M. (2005).
1670 Multiple Membrane Tethers Probed by Atomic Force Microscopy. *Biophysical Journal*,
1671 89(6), 4320–4329.
- 1672 Tabaei, S. R., Gillissen, J. J. J., Vafaei, S., Groves, J. T., & Cho, N.-J. (2016). Size-dependent,
1673 stochastic nature of lipid exchange between nano-vesicles and model membranes.
1674 *Nanoscale*, 8(27), 13513–13520. <https://doi.org/10.1039/C6NR03817D>
- 1675 Tellechea, E., Johannsmann, D., Steinmetz, N. F., Richter, R. P., & Reviakine, I. (2009). Model-
1676 Independent Analysis of QCM Data on Colloidal Particle Adsorption. *Langmuir*, 25(9),
1677 5177–5184. <https://doi.org/10.1021/la803912p>

- 1678 Tero, R. (2012). Substrate Effects on the Formation Process, Structure and Physicochemical
1679 Properties of Supported Lipid Bilayers. *Materials*, 5(12), 2658–2680.
1680 <https://doi.org/10.3390/ma5122658>
- 1681 Van Lehn, R. C., Ricci, M., Silva, P. H. J., Andrezzi, P., Reguera, J., Voitchovsky, K., Stellacci, F.,
1682 & Alexander-Katz, A. (2014). Lipid tail protrusions mediate the insertion of
1683 nanoparticles into model cell membranes. *Nature Communications*, 5(1), 4482.
1684 <https://doi.org/10.1038/ncomms5482>
- 1685 van Meer, G., & de Kroon, A. I. P. M. (2011). Lipid map of the mammalian cell. *Journal of Cell*
1686 *Science*, 124(1), 5.
- 1687 van Meer, G., Voelker, D. R., & Feigenson, G. W. (2008). Membrane lipids: Where they are and
1688 how they behave. *Nature Reviews Molecular Cell Biology*, 9(2), 112–124.
1689 <https://doi.org/10.1038/nrm2330>
- 1690 Veatch, S. L., & Keller, S. L. (2003). Separation of Liquid Phases in Giant Vesicles of Ternary
1691 Mixtures of Phospholipids and Cholesterol. *Biophysical Journal*, 85(5), 3074–3083.
- 1692 Vereb, G., Szöllösi, J., Matkó, J., Nagy, P., Farkas, T., Víggh, L., Mátyus, L., Waldmann, T. A., &
1693 Damjanovich, S. (2003). Dynamic, yet structured: The cell membrane three decades
1694 after the Singer–Nicolson model. *Proceedings of the National Academy of Sciences*,
1695 100(14), 8053 LP – 8058. <https://doi.org/10.1073/pnas.1332550100>
- 1696 Vist, M. R., & Davis, J. H. (1990). Phase equilibria of cholesterol/dipalmitoylphosphatidylcholine
1697 mixtures: Deuterium nuclear magnetic resonance and differential scanning
1698 calorimetry. *Biochemistry*, 29(2), 451–464. <https://doi.org/10.1021/bi00454a021>
- 1699 Vogel, V. (2006). MECHANOTRANSDUCTION INVOLVING MULTIMODULAR PROTEINS:
1700 Converting Force into Biochemical Signals. *Annual Review of Biophysics and*
1701 *Biomolecular Structure*, 35(1), 459–488.
1702 <https://doi.org/10.1146/annurev.biophys.35.040405.102013>

- 1703 Voinova, M. V., Rodahl, M., Jonson, M., & Kasemo, B. (1999). Viscoelastic Acoustic Response of
1704 Layered Polymer Films at Fluid-Solid Interfaces: Continuum Mechanics Approach.
1705 *Physica Scripta*, 59(5), 391. <https://doi.org/10.1238/Physica.Regular.059a00391>
- 1706 Wallace, E. J., Hooper, N. M., & Olmsted, P. D. (2006). Effect of hydrophobic mismatch on
1707 phase behavior of lipid membranes. *Biophysical Journal*, 90(11), 4104–4118.
1708 <https://doi.org/10.1529/biophysj.105.062778>
- 1709 Wargenau, A., & Tufenkji, N. (2014). Direct Detection of the Gel–Fluid Phase Transition of a
1710 Single Supported Phospholipid Bilayer Using Quartz Crystal Microbalance with
1711 Dissipation Monitoring. *Analytical Chemistry*, 86(16), 8017–8020.
1712 <https://doi.org/10.1021/ac5019183>
- 1713 Winkler, P. M., Campelo, F., Giannotti, M. I., & García-Parajo, M. F. (2020). Planar plasmonic
1714 antenna arrays resolve transient nanoscopic heterogeneities in biological membranes.
1715 *Proc.SPIE*, 11246. <https://doi.org/10.1117/12.2543726>
- 1716 Winkler, P. M., Regmi, R., Flauraud, V., Brugger, J., Rigneault, H., Wenger, J., & García-Parajo,
1717 M. F. (2017). Transient Nanoscopic Phase Separation in Biological Lipid Membranes
1718 Resolved by Planar Plasmonic Antennas. *ACS Nano*, 11(7), 7241–7250.
1719 <https://doi.org/10.1021/acsnano.7b03177>
- 1720 Yeagle, P. L. (1989). Lipid regulation of cell membrane structure and function. *The FASEB*
1721 *Journal*, 3(7), 1833–1842. <https://doi.org/10.1096/fasebj.3.7.2469614>
- 1722 Zou, S., & Johnston, L. J. (2010). Ceramide-enriched microdomains in planar membranes.
1723 *Current Opinion in Colloid & Interface Science*, 15(6), 489–498.
1724 <https://doi.org/10.1016/j.cocis.2010.06.003>
- 1725
- 1726
- 1727
- 1728

